

Dust reverberation mapping and light-curve modelling of Zw229-015

E. Guise¹,^{*} S. F. Hönig,¹ V. Gorjian,² A. J. Barth³,[†] T. Almeyda,^{1,4} L. Pei,³ S. B. Cenko,^{5,6} R. Edelson,⁷ A. V. Filippenko,⁸ M. D. Joner,⁹ C. D. Laney,^{9,10} W. Li,^{8,†} M. A. Malkan,¹¹ M. L. Nguyen¹² and W. Zheng⁸

¹Department of Physics and Astronomy, University of Southampton, Southampton SO17 1BJ, UK

²Jet Propulsion Laboratory, M/S 169-327, 4800 Oak Grove Drive, Pasadena, CA 91109, USA

³Department of Physics and Astronomy, 4129 Frederick Reines Hall, University of California, Irvine, CA 92697-4575, USA

⁴Department of Biological and Physical Sciences, South Carolina State University, Orangeburg, SC 29117, USA

⁵Astrophysics Science Division, NASA Goddard Space Flight Center, MC 661, Greenbelt, MD 20771, USA

⁶Joint Space-Science Institute, University of Maryland, College Park, MD 20742-2421, USA

⁷Department of Astronomy, University of Maryland, College Park, MD 20742-2421, USA

⁸Department of Astronomy, University of California, Berkeley, CA 94720-3411, USA

⁹Department of Physics and Astronomy, N283 ESC, Brigham Young University, Provo, UT 84602, USA

¹⁰Department of Physics and Astronomy, Western Kentucky University, 1906 College Heights Boulevard, Bowling Green, KY 42101, USA

¹¹Department of Physics and Astronomy, University of California, Los Angeles, CA 90095-1547, USA

¹²Department of Physics and Astronomy, University of Wyoming, Laramie, WY 82071, USA

Accepted 2022 August 25. Received 2022 August 20; in original form 2022 March 24

ABSTRACT

Multiwavelength variability studies of active galactic nuclei can be used to probe their inner regions that are not directly resolvable. Dust reverberation mapping (DRM) estimates the size of the dust emitting region by measuring the delays between the infrared (IR) response to variability in the optical light curves. We measure DRM lags of Zw229-015 between optical ground-based and *Kepler* light curves and concurrent IR *Spitzer* 3.6 and 4.5 μm light curves from 2010 to 2015, finding an overall mean rest-frame lag of 18.3 ± 4.5 d. Each combination of optical and IR light curve returns lags that are consistent with each other within 1σ , which implies that the different wavelengths are dominated by the same hot dust emission. The lags measured for Zw229-015 are found to be consistently smaller than predictions using the lag–luminosity relationship. Also, the overall IR response to the optical emission actually depends on the geometry and structure of the dust emitting region as well, so we use Markov chain Monte Carlo modelling to simulate the dust distribution to further estimate these structural and geometrical properties. We find that a large increase in flux between the 2011–2012 observation seasons, which is more dramatic in the IR light curve, is not well simulated by a single dust component. When excluding this increase in flux, the modelling consistently suggests that the dust is distributed in an extended flat disc, and finds a mean inclination angle of 49_{-13}^{+3} deg.

Key words: galaxies: active – galaxies: Seyfert – quasars: individual: Zw229-015.

1 INTRODUCTION

Active galactic nuclei (AGNs) are the very luminous central regions of galaxies that are powered by accretion on to a supermassive black hole (SMBH). Their emission is widely detectable over the entire observable electromagnetic spectrum and is variable over different time-scales, including intraday variability (\sim minutes to hours), short-term variability (\sim days to a few months), and long-term variability (several months to years).

Initially, it was proposed that the infrared (IR) emission solely originated in a circumnuclear dusty region, often referred to as the ‘dusty torus,’ that surrounds the accretion disc (AD) and SMBH. The torus was originally introduced to unify AGNs through its obscuration of optical emission depending on the orientation of the

AGNs with respect to the observer (e.g. Antonucci 1993), where type 1 and type 2 AGNs are, respectively, unobscured and obscured. This unification model has been successful in explaining many observed properties of AGNs; however, there has been evidence provided since that suggests the classical circumnuclear torus model is not solely able to explain the observed behaviour of all AGNs. For example, a torus-like structure might be missing from AGNs that are observed with little to no obscuration detected but are still missing the broad optical emission lines (dubbed ‘true’ type 2 AGNs), though such unobscured type 2 AGNs are believed to be rare objects (Shi et al. 2010). Furthermore, a second component that takes the form of an extended polar structure has also been observed to contribute to the overall IR emission (e.g. Raban et al. 2009; Hönig et al. 2012, 2013; Leftley et al. 2018). Hönig et al. (2012) suggest that the polar dust structure is the result of a radiatively driven dusty wind from the inner region of the torus. IR interferometry has been used to show that the mid-IR (MIR) emission predominantly originates in this polar region (e.g. Raban et al. 2009; Hönig et al. 2012, 2013; Leftley et al. 2018),

* E-mail: ella.guise@soton.ac.uk

† Deceased 12 December 2011.

and the hottest dust closest to the dust sublimation region in the equatorial disc component dominates the near-IR (NIR) emission (e.g. Swain et al. 2003; Kishimoto et al. 2009; Pott et al. 2010; Weigelt et al. 2012). However, IR interferometry is only possible for nearby, relatively bright AGNs, and therefore alternative indirect methods are necessary to study the location of the IR emission in the inner regions of more AGNs.

Reverberation mapping uses the assumption that changes in the variability of the emission from shorter wavelength ranges can drive changes in longer wavelength emission, therefore allowing the size of different components in the AGNs to be estimated from time delays between variability in the light curves (e.g. Blandford & McKee 1982; Peterson 1993). The inner radius of the dust emitting region, which is set by the dust sublimation temperature, can be estimated via dust reverberation mapping (DRM) as some of the optical emission produced in the AD is reprocessed by the surrounding dust and reemitted in the IR after a delay corresponding to the light-traveltime between the AD and dust emitting region (e.g. Barvainis 1987). Several studies of the dust reverberation radii of different AGNs have been performed, most using the NIR K band ($\sim 2.2 \mu\text{m}$) to define the dust sublimation radius of AGNs with redshift $z < 1$ (e.g. Nelson 1996; Minezaki et al. 2004; Suganuma et al. 2006; Koshida et al. 2014; Yoshii et al. 2014; Pozo Nuñez et al. 2015; Mandal et al. 2018, 2021; Ramolla et al. 2018; Minezaki et al. 2019) as it traces the peak of the hot dust emission at the inner radius with a dust sublimation temperature $T_{\text{sub}} \approx 1500 \text{ K}$ (e.g. Rieke & Lebofsky 1981; Barvainis 1987). Additionally, studies of DRM using longer wavelength IR light curves have been performed to further constrain the spatial information of the dust emitting region; for example, Lyu, Rieke & Smith (2019) combine MIR DRM lags from multiple quasars with $z < 0.5$ using WISE W1 ($\sim 3.4 \mu\text{m}$) and W2 ($\sim 4.5 \mu\text{m}$) bands with K -band results from the literature to infer the dust emission size ratios of $R_k: R_{W1}: R_{W2} = 0.6 : 1 : 1.2$. Similarly, Vazquez et al. (2015) performed DRM on the optical B and V and IR *Spitzer* channel 1 ($3.6 \mu\text{m}$) and *Spitzer* channel 2 ($4.5 \mu\text{m}$) light curves of NGC 6418, and measured lags between the optical continuum and the IR 3.6 and $4.5 \mu\text{m}$ with values of $37.2^{+2.4}_{-2.2}$ and $47.1^{+3.1}_{-3.1}$ d, respectively. They also measured a lag between the IR 3.6 and $4.5 \mu\text{m}$ light curves with a value of $13.9^{+0.5}_{-0.1}$ d. These studies find that the emission detected in the longer IR wavelengths of these AGNs is likely dominated by the blackbody peak of the emission from the cooler dust at larger radii; however, contributions to the MIR emission are also expected from the Rayleigh–Jeans tail of the hotter dust from the inner regions. In compact systems that lack the extended dust, it is therefore suggested by Hönig & Kishimoto (2011) that the emission at these wavelength ranges could predominately come from the hot dust Rayleigh–Jeans tail.

While DRM gives a good indication of the size of the dust emitting region, the overall delayed IR response to the optical emission actually depends on the structure and geometry of the dust emission region. While initially a smooth distribution of dust was assumed, it is now suggested to be distributed in clumps, both theoretically (e.g. Krolik & Begelman 1988; Tacconi et al. 1994) and with evidence from observations (e.g. Shi et al. 2006; Tristram et al. 2007). By modelling this clumpy dust distribution, the overall reprocessed IR light curves can be simulated. The IR response to a delta-function input continuum pulse represents the dust transfer function (DTF), which can be convolved with the driving optical light curve to give the portion of the IR light that corresponds to the reemitted optical continuum. Though the DTF is not directly measurable, simulated DTFs can be convolved with optical light curves and the resulting simulated IR light curve can be compared with the IR observations

to constrain properties, including the dust distribution, inclination angle, and dust reverberation radius of the AGNs. Several such models of the dust emitting region have been used to constrain the inner regions of AGNs; for example, Hönig & Kishimoto (2011) showed that the observed NIR K -band light curves of NGC 4151 could be well reproduced using observed optical V -band light curves convolved with simulated DTFs. Furthermore, Almeyda et al. (2017, 2020) modelled the IR response light curves to variations in the UV/optical using a torus reverberation mapping code (TORMAC), to explore geometrical and structural properties of the dusty torus.

Zw229-015¹ is a nearby Seyfert 1 galaxy at $z = 0.028$ (Falco et al. 1999). It is one of the brightest and most highly varying AGNs in the *Kepler* field, and was therefore selected as a target to be observed with *Kepler* during Quarters 4–17 (2010–2013), resulting in one of the highest quality, most complete optical light curves of any AGNs. Concurrent IR observations with *Spitzer* (2010–2015), along with additional optical observations from ground-based telescopes (2010–2015), make it ideal for DRM analysis over 5 yr. Multiple previous studies of Zw229-015 have been performed. Barth et al. (2011) measured a broad-line region (BLR) reverberation lag of $3.86^{+0.69}_{-0.24}$ d between the H β and V -band continuum light curves from 2010, and estimated a black hole mass of $\sim 10^7 M_{\odot}$. Smith et al. (2018) report a bolometric luminosity of $\log(L_{\text{Bol}} [\text{erg s}^{-1}]) = 44.11$ and an Eddington ratio of $L/L_{\text{Edd}} = 0.125$. Williams et al. (2018) modelled the BLR geometry and dynamics of Zw229-015 to estimate an inclination angle of the AD of $i = 32.9^{+6.1}_{-5.2}$ deg. Similarly, Raimundo et al. (2020) estimated an inclination angle of $i = 36.4^{+6.7}_{-6.4}$ deg, consistent with Williams et al. (2018) within the 1σ uncertainties. Furthermore, Mandal et al. (2021) performed DRM of Zw229-015 with observations between 2017 July and 2018 December, finding significant rest-frame lags between the V and K_s light curves of $20.36^{+5.82}_{-5.68}$ d.

The structure of this paper is as follows. In Section 2, we describe the observations and data reduction. We present the DRM analysis of Zw229-015 in Section 3, and in Section 4 we use Markov chain Monte Carlo (MCMC) modelling of the light curves to further constrain the dust reverberation lag and the geometry of the inner regions of the AGN. Section 5 discusses the results, and in Section 6 we present the summary and conclusions.

2 OBSERVATIONS AND DATA REDUCTION

2.1 Ground-based optical

Ground-based V -band photometric monitoring of Zw229-015 was carried out from 2010 June until 2014 December. Barth et al. (2011) presented the 2010 data, while the first five months of the 2011 data were included in the light-curve compilation presented by Pancoast et al. (2019). For this work, we carried out measurements of the 2010–2014 photometric data, including new measurements for the images used in these earlier studies, in order to ensure uniformity across the full time-series.

The data included here were obtained from four facilities: (1) The 0.9 m telescope of the BYU West Mountain Observatory (WMO) in Utah, (2) the 0.76 m Katzman Automatic Imaging Telescope (KAIT) at Lick Observatory (Filippenko et al. 2001), (3) the 1 m telescopes of the Las Cumbres Observatory (LCO) located at McDonald Observatory (Brown et al. 2013), and (4) the 2 m Faulkes Telescope North (also a part of the LCO network) located at Haleakala Observatory

¹ $\alpha = 19^{\text{h}}05^{\text{m}}25^{\text{s}}.939$, $\delta = +42^{\circ}27'39''.65$ (J2000)

using the Spectral camera. Exposure times ranged from 60 s to 300 s for individual integrations, and two or more exposures per night were usually taken at a given facility in order to increase the signal-to-noise ratio (S/N) and facilitate cosmic ray rejection. The previously published measurements of the 2010 data (Barth et al. 2011) included a small number of additional observations obtained at other facilities, but those images were not included for the light-curve measurements presented here.

Images were processed by the standard reduction pipeline for each facility, including bias subtraction and flat-fielding. Photometry was carried out using the IDL-based aperture photometry pipeline described by Pei et al. (2014). This procedure automatically identifies the position of the AGNs and a set of comparison stars in each image based on their coordinates, and uses routines in the IDL Astronomy Users' Library (Landsman 1995) to measure their instrumental magnitudes. Photometry was obtained in a circular aperture of radius 4 arcsec, with a sky annulus between 10 arcsec and 20 arcsec. For each image, a shift was applied to the measured instrumental magnitudes in order to minimize the scatter in the comparison star light curves. When multiple exposures were taken on a single night at a given facility, the resulting measurements were combined using a weighted average to obtain a single photometric data point. Small discrepancies between the magnitude scales of the different telescopes were removed by designating the WMO light curve as the reference, and applying additive offsets to the light curves of Zw 229-015 from the other telescopes to yield the best average match to the WMO magnitudes on nights with observations in common between WMO and the other facilities. Finally, the light curve was placed on a calibrated *V* magnitude scale (in the Vega system) using the comparison-star calibrations from Barth et al. (2011). Since the photometry was carried out using different methods than those applied for the previous measurements of the 2010 and 2011 data, there are small differences between the light-curve data presented here and the measurements previously presented by Barth et al. (2011) and Pancoast et al. (2019).

2.2 Kepler

The pipeline processed *Kepler* light curves are not appropriate for AGN monitoring (e.g. Edelson et al. 2014; Kasliwal, Vogeley & Richards 2015). This is broadly due to the fact that the *Kepler* pipeline processing is optimized for small flux changes due to exoplanet transits and so tends to minimize large-scale variations that can appear in AGN light curves, and so separate reductions need to be undertaken for AGNs. We have used the light curve produced by Edelson et al. (2014) which is extracted directly from the 2D pixel data using different extraction masks than the pipeline. This process gives a significantly different result than the pipeline. For details of the process, please see Edelson et al. (2014). The ~ 30 min cadences were of much finer resolution than was necessary for the upcoming analysis, so the multiple measurements from each epoch were combined to provide a single photometric data point. The following sections show that the *Kepler* light curve matches the ground-based optical light curve very well both in direct comparison and the reverberation mapping results.

2.3 Spitzer

The *Spitzer Space Telescope* (Werner et al. 2004) observations were taken with the Infrared Array Camera (IRAC; Fazio et al. 2004) scheduled between 2010 August 6 and 2015 January 26 (UTC) with an average spacing of 3 d between observations; moreover,

observations were not taken <2.5 d apart nor >3.5 d apart. These limits were set to allow maximum flexibility of scheduling for *Spitzer's* other programs; a narrower time window would force an 'either/or' choice by the schedulers, thereby endangering the continuous coverage of Zw229-015.

For the first two epochs of data (PID 70119, 80148), we requested data only at the $3.6 \mu\text{m}$ band, thinking that the $4.5 \mu\text{m}$ -band data would show variability on a longer time-scale than our observing window. We then added the $4.5 \mu\text{m}$ data in the third and fourth epochs (PID 90144, 10125), as preliminary analysis of the time variability at the shorter wavelength showed the variability time-scales to be significantly less than our observing window.

In order to attain the highest precision in the light-curve data, we followed the procedures in the IRAC Instrument Handbook² to reduce interpixel and intrapixel systematic errors. Based on analysis of standard stars used for calibration, it was determined that having at least 16 dithers with IRAC at the medium spacing would provide ~ 1 per cent photometry for a large field around the AGNs.

Fig. 1 shows a stacked image obtained at $3.6 \mu\text{m}$ by *Spitzer* and another at *V* obtained by the WMO and first presented by Barth et al. (2011). IR photometry was acquired in a 4 pixel (2.4 arcsec) radius aperture with a background annulus of 12–20 pixels (7.2 arcsec–12 arcsec). The aperture radius was chosen to be the region of the image most dominated by the AGNs, and the sky annulus was chosen to subtract a significant portion of the host-galaxy light without subtracting any of the extended point spread function from the AGNs. The quality of the data was such that there was no need to make relative measurements to the stars near the AGNs to generate the light curves.

The uneven gaps between the *Spitzer* light curves (Fig. 2) arose because of a mismatch between the visibility of Zw229-015 to the telescope and the proposal cycles for *Spitzer*.

2.4 Light-curve variability

Fig. 2 shows the optical and IR light curves of Zw229-015 in 2010–2015, with observation seasons separated by the dotted grey lines, and with overall magnitude variations (brightest – dimmest magnitude) of each light curve of $|\Delta_{\text{ground}}| \approx 0.6$ mag, $|\Delta_{\text{Kepler}}| \approx 0.6$ mag, $|\Delta_{\text{Spitzer } 1}| \approx 0.9$ mag, and $|\Delta_{\text{Spitzer } 2}| \approx 0.2$ mag. The short-term variability (i.e. variability over time-scales of days to months) of the individual seasons in each light curve are approximately consistent for the entire light curves, with mean overall magnitude variations of ~ 0.3 , ~ 0.4 , ~ 0.2 , and ~ 0.1 mag in the ground-based optical, *Kepler*, and *Spitzer* channel 1 and 2 light curves, respectively. Additionally, underlying long-term variability (i.e. variability over time-scales of several months to years) can be seen in the light curves, especially those that are observed in 2011–2013 as the object gets brighter, with a change of mean apparent magnitude of ~ 0.2 , ~ 0.2 , and ~ 0.6 mag in the ground-based optical, *Kepler*, and *Spitzer* channel 1 light curves, respectively.

The light curves in Fig. 2 were then converted into fluxes for the upcoming analysis. It is worth noting that the observations of Zw229-015 also likely contain a substantial amount of flux from the host galaxy, the amount of which varies for each survey; however, this host-galaxy flux is assumed to be constant over the entire observational period. For consistency between the optical light curves in Fig. 2, a constant flux of 3.7 mJy corresponding to the mean of the

² <https://irsa.ipac.caltech.edu/data/SPITZER/docs/irac/>

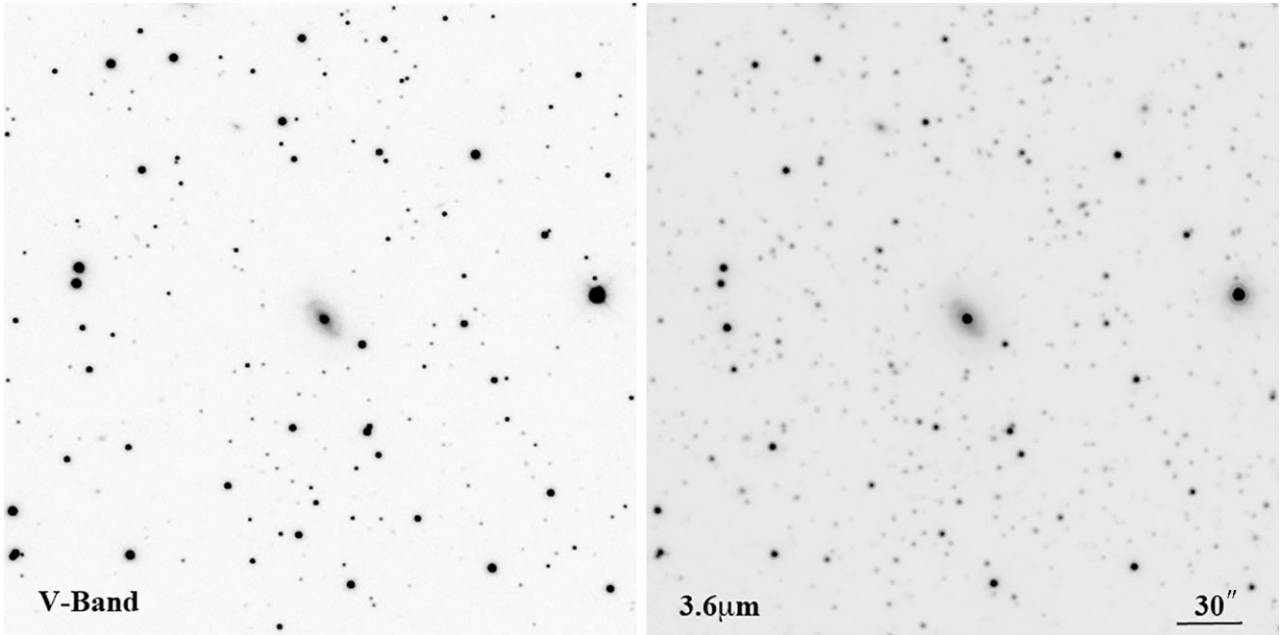


Figure 1. Stacked images of Zw229-015 from ground-based optical (V-band) imaging from the WMO (Barth et al. 2011) and the IR (3.6 μm) image from the *Spitzer Space Telescope*.

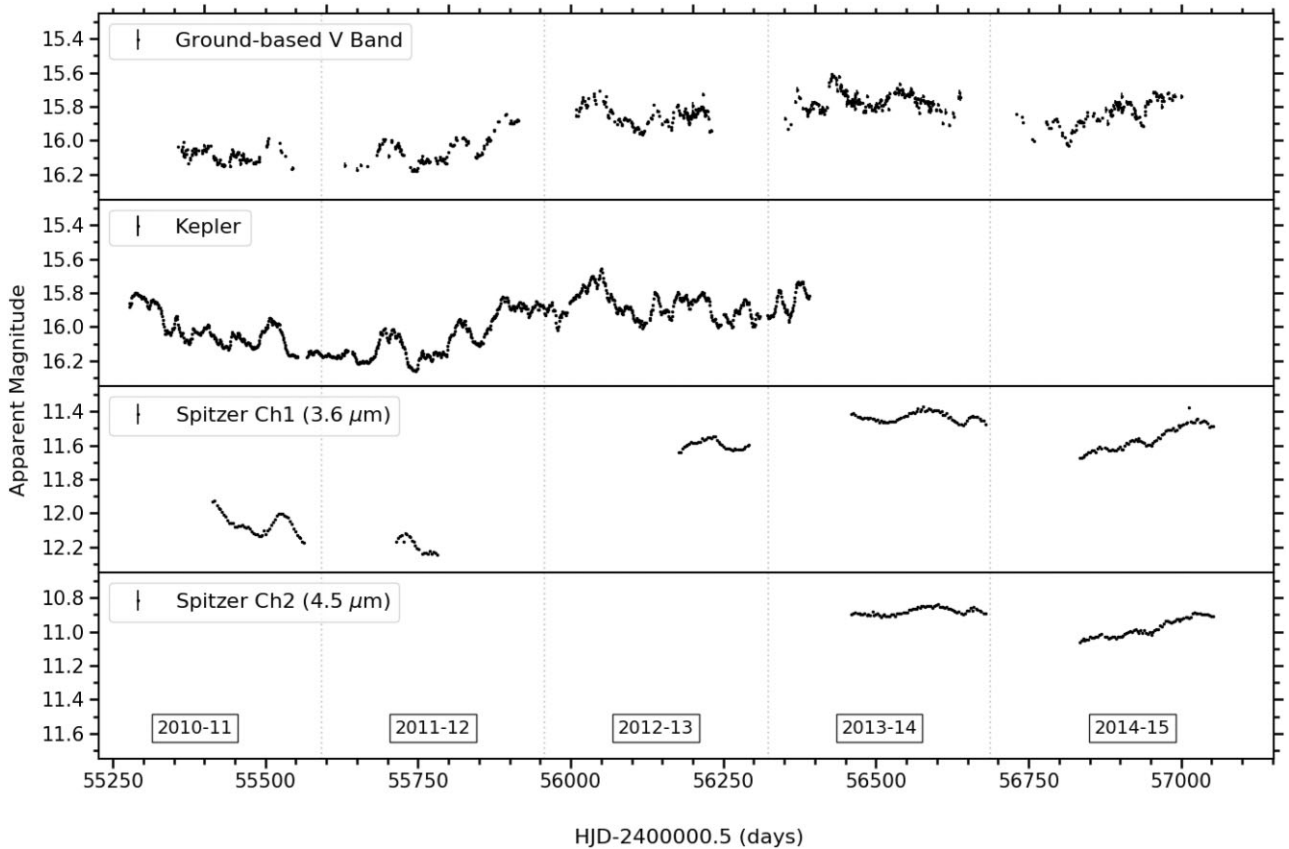


Figure 2. Light curves of Zw229-015 from the ground-based optical telescopes and *Kepler*, and from IR *Spitzer* Channel 1 (3.6 μm) and *Spitzer* Channel 2 (4.5 μm). The points represent observations, and the grey dotted lines separate each observation season.

difference between the overlapping ground-based *V*-band and *Kepler* observations was subtracted from the *Kepler* observations.

3 DUST REVERBERATION MAPPING

Potential reverberation lags between the optical and IR light curves of Zw229-015 were recovered using the cross-correlation function (CCF), which computes a correlation value between the light curves for a range of potential lags (e.g. Peterson 1993). This requires the light curves to be continuous; therefore, they were interpolated to simulate data between observations using the structure function (SF), which measures the fractional change in flux of the observations that are separated by given time intervals (e.g. Suganuma et al. 2006, Emmanoulopoulos, McHardy & Uttley 2010).

Interpolation can lead to large portions of simulated data between observation seasons, which in turn creates uncertainties in the cross-correlation analysis. Therefore, to reduce the impact of the interpolations, two methods of interpolated cross-correlation function (ICCF; e.g. Peterson et al. 1998) were compared. The first method used a standard-ICCF (S-ICCF), in which both light curves were interpolated with 1 d cadences before cross-correlating. This method utilized all available observations in both light curves, but also treated the interpolated data equally with observations and could therefore decrease the reliability of the result. The second method only interpolated one of the light curves at a time, and the data corresponding to the epochs of observation of the second light curve plus a range of potential lags were extracted and cross-correlated (Guise et al. 2022). This meant less interpolated data were included, especially when cross-correlating multiple observation seasons with months-long gaps between them, but did not use all available data. This method would therefore need to be performed twice, interpolating each of the light curves, which will be referred to as the modified-ICCF (M-ICCF) and reverse modified-ICCF (RM-ICCF) methods, respectively.

3.1 Optical–IR cross-correlation results

Each individual season of each combination of the optical and IR light curves, as well as the entire overlapping light curves of Zw229-015, were interpolated and cross-correlated using the methods discussed above. The light curves were interpolated using the SF, filling in the missing data in a random order to estimate the variability from different time separations, therefore this method was repeated 10 000 times for each combination of light curves to decrease the impact of the interpolated data in each instance on the cross-correlation results. When cross-correlating the light curves covering more than one observation season, the light curves were first detrended as explained in Appendix B1 (supplementary material), to remove the influence of long-term variations (that were over time-scales much greater than expected for DRM; e.g. Clavel, Wamsteker & Glass 1989; Glass 1992; Suganuma et al. 2006) from the CCFs (e.g. Welsh 1999).

Each CCF was tested with a lag range of ± 100 d owing to the length of the individual observation seasons, except for the season starting 2011, in which the *Spitzer* 1 light curve only covers a period of 67 d and hence was only tested with a range of ± 60 d, and the season starting in 2012 in the ground-*Spitzer* 1 CCF, in which the light curves only have overlapping periods of observation of 54 d, and hence was only tested with lags between ± 50 d. Potential lags that were measured from peaks on the CCFs were considered positive detections if the CCF values were > 0.5 , as most non-zero peaks in the autocorrelation functions (ACFs) had values smaller than this, with

the exception of the edges of some ACFs, and the M-ICCF ACFs of seasons starting 2010, 2012, and 2014 which display secondary peaks between ± 55 and 70 d as discussed below. These possible lags were labelled on the plot, with the uncertainties calculated as the standard deviations of the peak of the CCF for each interpolation around the mean CCF.

Figs 3 and 4 contain the mean CCFs and ACFs of the entire overlapping periods of the ground-*Spitzer* 1, *Kepler*-*Spitzer* 1 and ground-*Spitzer* 2 light curves, and the CCFs and ACFs of some of the individual observation seasons of the ground-*Spitzer* 1 light curves, respectively. Appendix B2 (supplementary material) contains the remaining individual season CCFs of each combination of optical and IR light curve.

The most consistent possible lag detected occurs between ~ 5 and 30 d. As there are no corresponding peaks in the ACFs at these lags, it is likely not affected by the variability of each light curve individually and instead is a potential delay between the optical and IR light curves. A positive detection of this lag is recorded in at least one method in each season and in the entire combined light curves (with the exception of the ground-*Spitzer* 2 2013 season CCF which is discussed in Appendix B2.1) (supplementary material); however, it is not detected in all methods of each observation season. For example, this lag is not detected in the S-ICCF method in the entire overlapping ground-*Spitzer* 1 CCFs in Fig. 3(a), or in the S-ICCF and M-ICCF methods of the entire overlapping *Kepler*-*Spitzer* 1 CCFs in Fig. 3(b); however, this is likely due to interpolations of the *Spitzer* 1 light curve, including in the large gap in observations between HJD 55800 and 56150.

Furthermore, potential lags between ~ 55 and 80 d are detected in multiple plots, although less frequently than the ~ 20 d lag. For example, they are present in either the M-ICCF or RM-ICCF methods of each combination of optical–IR in the 2010 and 2014 CCFs as shown in Figs 4(a) and (c), respectively. The shape of the light curves in these seasons could be impacting the CCFs, however, as the corresponding optical ACF for each CCF that detects this lag has a secondary peak at ~ 55 –70 d. For example, the lag is detected in the RM-ICCF method of the 2010 season ground-*Spitzer* 1 CCF and in the corresponding ground ACFs there is a relatively high peak at $\sim \pm 60$ d, with an ACF value of ~ 0.7 . This means that the *Spitzer* 1 light curve would correlate with the ground light curve at the lag τ and $\tau + 60$ d (i.e. if $\tau \approx 20$ d, then $\tau + 60 \approx 80$ d). Furthermore, the M-ICCF and RM-ICCF methods of the 2014 season CCFs display multiple peaks separated by ~ 50 –60 d, as shown in Fig. 4(c) for example, which could also be due to the shape of the optical and IR light curves in this season as they follow an increase with multiple distinct bumps separated by ~ 50 –60 d that correlate with each other. This correlation can be seen in the M-ICCF ACFs of both light curves by the peaks at $\sim \pm 60$ d with ACF values of ~ 0.6 in the ground optical and 0.9 in the *Spitzer* 1 and 2. Therefore, as this ~ 55 –80 d lag has corresponding peaks in the optical ACFs, it is unlikely to be due to a delay between optical and IR light curves, but instead aliasing in the light curves of certain seasons. Appendix B3 (supplementary material) explores whether this is a periodicity in the optical light curves, but finds that it appears to be a sampling effect as it only occurs for the overlapping light-curve periods and not on longer light curves.

Finally, possible lags between ~ -100 and -90 d are displayed in multiple methods and seasons – for example, in all methods of the ground-*Spitzer* 1 2010 season, and the M-ICCF and RM-ICCF methods of ground-*Spitzer* 1 in the 2013 and 2014 seasons displayed in Fig. 4. These peaks in the CCFs occur only owing to a small number of overlapping data points, so are deemed less significant than other

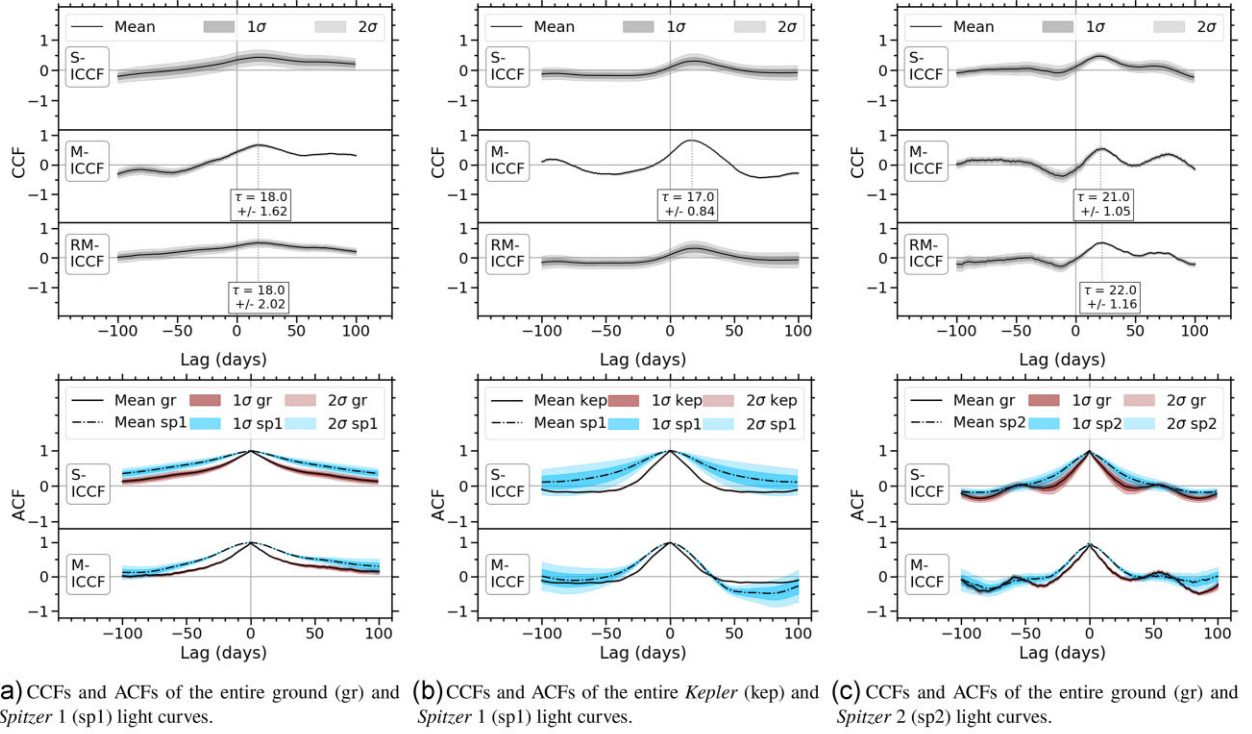


Figure 3. CCF and ACF of each combination of the optical and IR light curves of Zw229-015 over the entire overlapping observational periods, after subtraction of long-term variability. Here, M-ICCF refers to interpolating the optical light curve and RM-ICCF refers to interpolating the IR light curve.

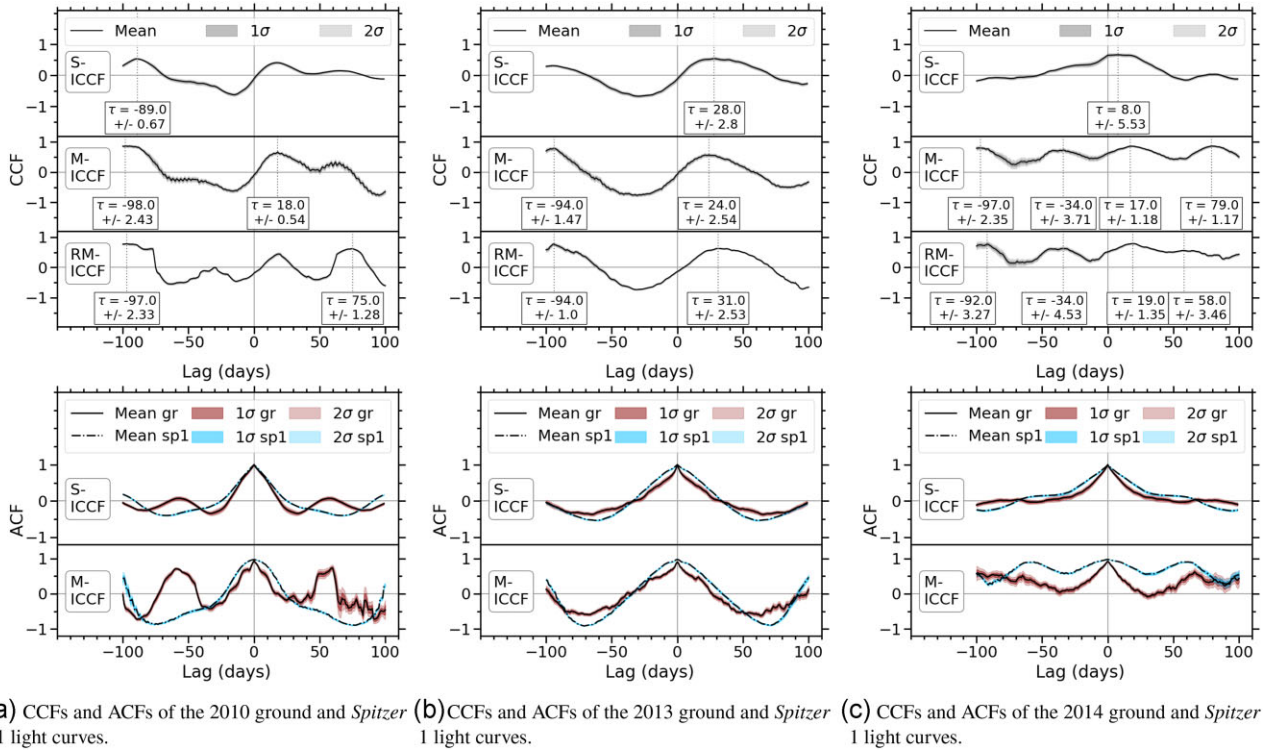


Figure 4. CCF and ACF of the ground optical (gr) and *Spitzer* 1 (sp1) light curves for some of the individual observation season light curves of Zw229-015. Here, M-ICCF refers to interpolating the ground and RM-ICCF refers to interpolating the *Spitzer* 1 light curve.

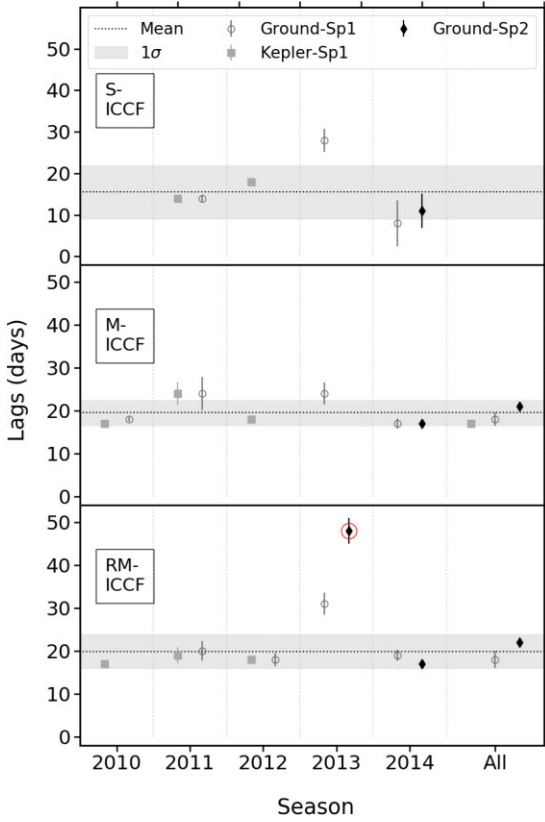


Figure 5. The lags measured between the optical and IR light curves of Zw229-015 between 0 and 50 d for each combination of optical (ground and *Kepler*) and IR [*Spitzer* 1 (sp1) and *Spitzer* 2 (sp2)] for each season and using each CCF method (S-ICCF, M-ICCF, and RM-ICCF). The ground-*Spitzer* 2 RM-ICCF is circled in red as a possible outlier, and is excluded from the mean calculation.

possible lags. Additionally, similar correlations are present in at least one of the corresponding ACFs, which further implies that the peak is not necessarily due to a lag between light curves but impacted by aliasing.

As the ~ 20 d lag was deemed to be most significant, it was further compared in each season and for each combination of optical and IR light curves in Fig. 5. This lag is found consistently with values between 8 and 30 d, with a mean of 18.8 ± 4.6 d (or 19.8 ± 7.1 d including the 2013 season RM-ICCF lag). The mean of the individual methods, S-ICCF, M-ICCF and RM-ICCF, are 15.5 ± 6.4 , 19.5 ± 2.9 , and 19.9 ± 4.0 d (or 22.5 ± 8.9 d including the 2013 season RM-ICCF lag), respectively, which are all consistent within 1 standard deviation of each other, and the mean of each combination of optical and IR light curve are 19.8 ± 5.7 , 18.0 ± 2.5 , and 17.6 ± 3.9 d (or 22.7 ± 11.9 d including the 2013 season RM-ICCF lag) for the ground-*Spitzer* 1, *Kepler-Spitzer* 1, and ground-*Spitzer* 2, respectively, which are also within 1 standard deviation of each other. The 2013 season in the RM-ICCF method shows a longer lag between 30 and 50 d, which is explored further in Appendix B2.1 (supplementary material).

3.2 *Spitzer* 1 - *Spitzer* 2 cross-correlation results

The overall combined *Spitzer* light curves were also cross-correlated using the methods described to measure potential lags between the 3.6 and 4.5 μm emission regions, as displayed in Fig. 6, and in

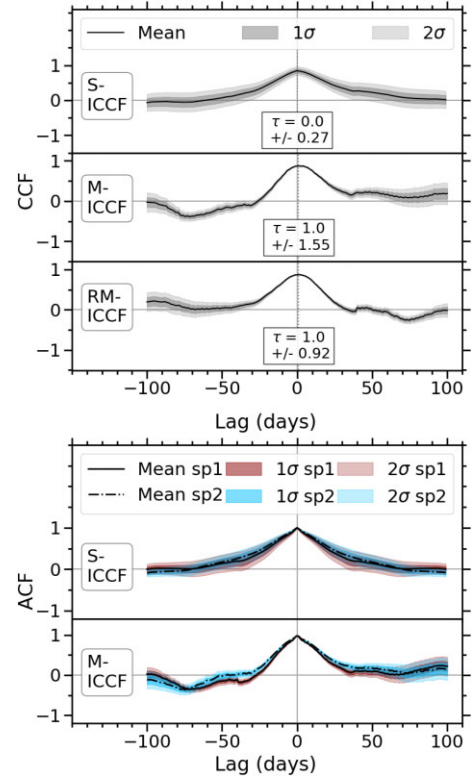


Figure 6. CCF and ACF of the *Spitzer* 1 (sp1) and *Spitzer* 2 (sp2) light curves for the entire overlapping light curves of Zw229-015.

Appendix B2 (supplementary material) for the individual seasons. The most consistent lag is measured with value between ~ 0 and 5 d, and is detected in each CCF, with a mean of 1.8 ± 1.7 d. Additional lags are measured in the M-ICCF methods of the 2014 season with values of ~ 47 d and $\sim \pm 100$ d; however, as similar peaks are found in the M-ICCF ACFs at this time, the peak in the CCFs is likely a result of the shape of the light curves and not a delay between the 3.6 and 4.5 μm emission.

4 LIGHT-CURVE MODELLING

The light curve of the reprocessed optical emission into the IR at time t can be expressed as a convolution of the optical light curve with a DTF (Peterson 1993),

$$f_{\text{IR}}^{\text{rep}}(t) = \int_{-\infty}^{+\infty} \Psi(\tau') f_{\text{opt}}(t - \tau') d\tau'. \quad (1)$$

Here, $f_{\text{opt}}(t - \tau')$ is the optical light curve at an earlier time $t - \tau'$, τ' is an arbitrary delay, $\Psi(\tau')$ is the DTF, and $f_{\text{IR}}^{\text{rep}}(t)$ is the reprocessed IR light curve at time t :

$$f_{\text{IR}}^{\text{rep}}(t) = f_{\text{IR}}^{\text{obs}}(t) - f_{\text{IR}}^{\text{disc}}(t), \quad (2)$$

where $f_{\text{IR}}^{\text{obs}}(t)$ is the total observed IR light curve at time t , and $f_{\text{IR}}^{\text{disc}}(t)$ is the contribution to the observed IR light curve from the AD at time t , which is estimated from

$$f_{\text{IR}}^{\text{disc}}(t) = f_{\text{opt}}(t) \left(\frac{\nu_{\text{IR}}}{\nu_{\text{opt}}} \right)^{\alpha_{\nu}}, \quad (3)$$

where $f_{\text{opt}}(t)$ is the optical flux at time t , ν_{IR} and ν_{opt} are, respectively, the effective frequencies of the IR and optical filters, and α_{ν} is the

power-law index which is set to the expected value of $\alpha_v = 1/3$ in the standard accretion-disc model (Shakura & Sunyaev 1973).

The DTF describes how emission from the optical continuum is reprocessed into the observed IR emission. It depends on the geometry and structure of the dust emission region, and as such, can be used to provide further information on the inner regions of the AGNs that cannot be spatially resolved. However, the DTF is not directly measurable, and finding a unique solution for it in equation (1) would require high-quality data; thus, in this paper, it is estimated by first simulating the distribution of the dust in the inner regions of the AGN.

4.1 Simulating dust transfer functions

Currently, the dust distribution in the inner regions of the AGNs can only be spatially resolved using interferometry on relatively bright, nearby AGNs. However, it can also be estimated using dust reverberation time delays, as dust at different locations correspond to different light-traveltimes to the observer, so the overall IR dust response to the optical emission is made up of a range of lags.

For this paper, 10 000 dust clouds are randomly distributed as follows. First, in the equatorial plane, the clouds are distributed following a radial power law with index α , as given in equation (4) below, and are uniformly distributed with azimuthal angle (ϕ) between 0 and 2π . Steep radial power-law indices (i.e. small values of α) correspond to a compact object, while in shallow radial brightness distributions, the dust is extended as shown in Appendix C1 (supplementary material). The heights of the dust clouds above the equator (h) are distributed following a vertical scale height power law with index β , as given by equation (5) below, where values of $\beta = 0$ correspond to a flat disc, $\beta = 1$ is a flared disc of constant ratio of height to radius, and $\beta > 1$ follows an outflow-like distribution as shown in Appendix C1 (supplementary material). The sizes of the dust clouds are assumed to be much smaller than the size of the overall dust distribution, so the dust clouds are treated as points in this model.

$$r \propto \left(\frac{r'}{r_{\text{sub}}} \right)^\alpha, \quad (4)$$

where r' is the distance of each dust cloud from the centre and r_{sub} is the dust sublimation radius, and

$$h \propto r^\beta, \quad (5)$$

where r is the radial position of each dust particle from equation (4).

These optically thick dust clouds are assumed to be directly heated from the AGNs; thus, only the side facing the AGNs is illuminated while the far side is not. The observed emission therefore depends on the angle (ψ) that describes the dust cloud's position relative to the equatorial plane and relative to the observer,

$$\cos \psi = \cos \theta \cos \phi \sin i + \sin \theta \cos i, \quad (6)$$

where θ is the complement of the polar angle and i is the inclination angle of the system. The inclination angle affects the delay maps as shown in Appendix C1 (supplementary material), as when the disc is tilted (e.g. represented by an angle of $i = 69^\circ$) the far-side clouds have larger delays and the near-side clouds have smaller delays relative to the dust clouds in a face-on disc (i.e. $i = 0^\circ$).

As only the side of the dust cloud that is facing the AGNs is illuminated, the fraction of a dust cloud's illuminated surface that is then visible to the observer (κ) is estimated from

$$\kappa = 0.5 (1 - \cos \psi), \quad (7)$$

where an angle of $\psi = 180^\circ$ corresponds to the entire illuminated side of the dust cloud being visible to the observer, while for an angle of $\psi = 0^\circ$, the entire non-illuminated side is visible to the observer. An example of the illumination is displayed in Appendix C1 (supplementary material).

The dust clouds are assumed to radiate as blackbodies, and after accounting for the illumination effects, the DTF can be estimated from the combined emission response of each dust cloud [calculated using the Planck function, $B_\nu(T(r))$, for temperature $T(r)$ at radial distance r given by equation (8)] to a delta-function input continuum pulse,

$$T(r) = T_{\text{sub}} \left(\frac{r}{r_{\text{sub}}} \right)^{\frac{-2}{4+\gamma}}, \quad (8)$$

where $T_{\text{sub}} = 1500$ K is the sublimation temperature, and γ is the dust IR opacity power-law index, which is set to 1.6 to correspond to standard interstellar dust material dust grains (Barvainis 1987).

Using this method, a grid of DTFs was simulated for each IR wavelength, for a range of radial power-law indices $-5.5 \leq \alpha \leq -0.5$, a range of vertical scale height power-law indices $0.05 \leq \beta \leq 2.05$, and a range of inclination angles $0^\circ \leq i \leq 69^\circ$. The DTFs are calculated over (0–16) τ , where τ corresponds to the projected light-traveltime between the source of the optical and IR emission. Note that this model includes a number of simplifying assumptions in the distribution of dust and emission from the dust clouds that is observed, and excludes additional complexities that will likely effect the simulated DTFs, which will be discussed in more detail in Section 5.2.1.

4.2 MCMC modelling of the DTFs and light curves

To estimate the DTF that best describes the IR response of an AGN to the driving optical light curve, and as such further constrain properties of the inner regions of the AGNs, MCMC modelling is used to fit models of the IR light curve to the IR observations. This modelling is performed on the relative light curves, $g_i(t) = f_i(t)/\langle f_i(t) \rangle - 1$ ($i = \text{IR, opt}$), where $\langle f_i(t) \rangle$ is the mean flux of the light curves, $f_i(t)$, over the entire observational period being modelled. As most AGNs (excluding blazars) will vary annually in the IR by ~ 10 per cent (e.g. Lyu, Rieke & Shi 2017), the uncertainty in the IR light curves is set to 1 per cent of the flux, to prevent the model from trying to overfit the shorter time-scale variations (i.e. the nightly/weekly variations).

An MCMC search is performed over the parameters described in Table 1 to find the DTFs that result in reasonable fits of the simulated IR light curve to observations. These parameters include the radial power-law index, vertical scale height power-law index, inclination angle, and time lag that describe the parameter space of the DTF grids created in the previous section. They also include parameters such as the optical–IR amplitude conversion factor, w_{eff} , which is a scaling factor of the amplitudes of the transfer functions to account for uncertainties such as different amounts of host-galaxy contributions in the different light curves or the accretion-disc subtraction in the IR light curves, and an additional offset that could arise owing to using relative light curves.

The driving optical light curve that is convolved with the best-fitting DTF needs to be uniformly sampled; hence, resampled light curves were found by linearly interpolating the observations with a cadence of 4 d. While the mean of the interpolations could be used as the input optical light curve, they could underestimate the variability within the seasonal gaps, so instead the input optical light curves are treated as free model parameters with a prior range that is constrained

Table 1. Descriptions of the parameters of the MCMC modelling that are used to find the best-fitting DTF and simulate the IR light curves.

Parameter	Definition	Priors range
Radial power-law index, α	Power-law index that is used to describe the radial distribution of dust	$-5.5 \leq \alpha \leq -0.5$
Vertical scale height power-law index, β	Power-law index that is used to describe the vertical distribution of the dust above the equator	$0.05 \leq \beta \leq 2.05$
Time lag (d), τ	The projected time delay between optical and IR light curves	$5 \leq \tau \leq 30$ d
Inclination angle (deg), i	The angle between the system and line of sight of the observer	$1 \leq i \leq 69$
Optical–IR amplitude conversion factor, w_{eff}	The scaling factor of the amplitudes of the DTFs to account for uncertainties within the light curves, including different amounts of host-galaxy flux in the different observations and accretion-disc subtraction	$0.2 \leq w_{\text{eff}} \leq 11$
Offset	Additional offset between relative light curves	$-0.2 \leq \text{Offset} \leq 0.2$
Resampled relative optical light curve	As the observed optical light curves are not necessarily evenly sampled, they are interpolated and then treated as free parameters to find the best-fitting optical light curve that, when convolved with the DTF, best fits the IR observations.	Interpolated optical light curve \pm the 1σ uncertainties at that point

by the data, and a simultaneous MCMC search is performed to also find the best optical light curve that when convolved with the DTF best fits the IR observations.

4.3 Results of MCMC light-curve modelling

4.3.1 Modelling the entire light curves

Each combination of optical and IR light curve of Zw229-015 was modelled using the methods described above to attempt to further constrain the inner regions of the AGNs. The MCMC modelling was performed using 64 chains, each with a length of 50 000 iterations, which was sufficient for the parameters to converge. The range of priors for each parameter is listed in Table 1, where the time lag (for example) is constrained by the results of the DRM in Section 3. The quality of the fit is measured using the reduced χ^2 to compare the simulated light curves to the observations.

Initially, the entire overlapping light curves were modelled for each combination of optical and IR; for example, Fig. 7 displays the model that corresponds to the maximum of the posterior distribution for the entire *Kepler-Spitzer* 1 light curves. It can be seen here that the overall variability trends of the simulated IR light curve of the order of several months to years fits the observations relatively well; however, the shape of the simulated IR light curve for the individual seasons deviates from the observations, specifically in the 2011 and 2012 seasons where the amplitude of variability appears to be overestimated. A dramatic increase in flux occurs between the 2011 and 2012 seasons, which is greater in the IR than optical and could affect the modelling, so to investigate this, only the 2010–2011 seasons were modelled in Fig. 8. It can be seen that this simulated light curve follows the shape of the 2011 season substantially better than Fig. 7, both by eye and by the reduced χ^2_{IR} , although the flux is now underestimated at the start of the 2010 season. Furthermore, the peak of the simulated light curve in Fig. 8 at \sim HJD 55525 matches the observations better than Fig. 7. The means of the parameters that correspond to the best-fitting DTFs in each of the 64 MCMC chains are compared in Table C1 for the *Kepler-Spitzer* 1 model over 2010–2011 and 2010–2012, and are shown to be consistent for the radial power-law index, vertical scale height power-law index, and inclination angle. However, the amplitude conversion factor is larger for the 2010–2012 simulated light curves, which explains why the variability of the 2011 season appears overestimated. Also, the time

lag between optical and IR emission is \sim 20 d in the 2010–2012 model compared to the \sim 10 d found by only fitting the simulated light curves to the 2010–2011 seasons, which again could explain why the simulated peak at \sim HJD 55525 is later than the observations in Fig. 7.

Furthermore, in Fig. 9, the best-fitting DTF found for Fig. 8 has been convolved with the entire observed *Kepler* light curve. Here, the flux of the simulated light curve in the 2012 season is underestimated; however, the shape matches the observations well, which can be further seen in Fig. C7. This suggests that the increase in flux between the 2011 and 2012 seasons is not well modelled by a single dust component; thus, to exclude any effect from the dramatic increase in flux going forward, the entire light curves are instead separated into the 2010–2011 seasons and the 2012–2014 seasons when modelling light curves that cover multiple seasons. The simulated ground-*Spitzer* 1 and ground-*Spitzer* 2 light curves are discussed in Appendix C3 (supplementary material).

Table 2 contains the corresponding mean and 1σ uncertainties for each parameter in the MCMC modelling that describe the best-fitting DTF in each combination of optical and IR light curves. It can be seen that the results for the radial power-law index and vertical scale height power-law index are consistent over the different combinations of light curves, as each model suggests a shallow radial power-law index with a mean of $\alpha = -0.52 \pm 0.01$ and a small vertical scale height power-law index with a mean of $\beta = 0.14 \pm 0.06$. The inclination angles are less well constrained in each model than the other parameters, demonstrating large 1σ uncertainties of $\sim 20^\circ$ – 30° , but they return an overall mean of $i = 49.1^\circ \pm 2.1^\circ$. Differences in the time lag can be seen depending on the seasons modelled, as the ground-*Spitzer* 1 and *Kepler-Spitzer* 1 light curves over the 2010–2011 seasons find lags of \sim 10 d, while the ground-*Spitzer* 1 and ground-*Spitzer* 2 light curves over the 2012–2014 and 2013–2014 seasons (respectively) find longer time lags that tend towards the upper limit of the prior range, with values of $\tau \approx 25$ – 30 d. This gives an overall mean value of $\tau = 18.5 \pm 9.2$ d, but could also imply that the delay between light curves is increasing with time. It is worth noting that the small uncertainties returned for some of the parameters of these modelled IR light curves are likely a product of the simplified clumpy dust models used to simulate the DTFs, and the exclusion of further complexities that can affect the DTFs which are discussed further in Section 5.2.1.

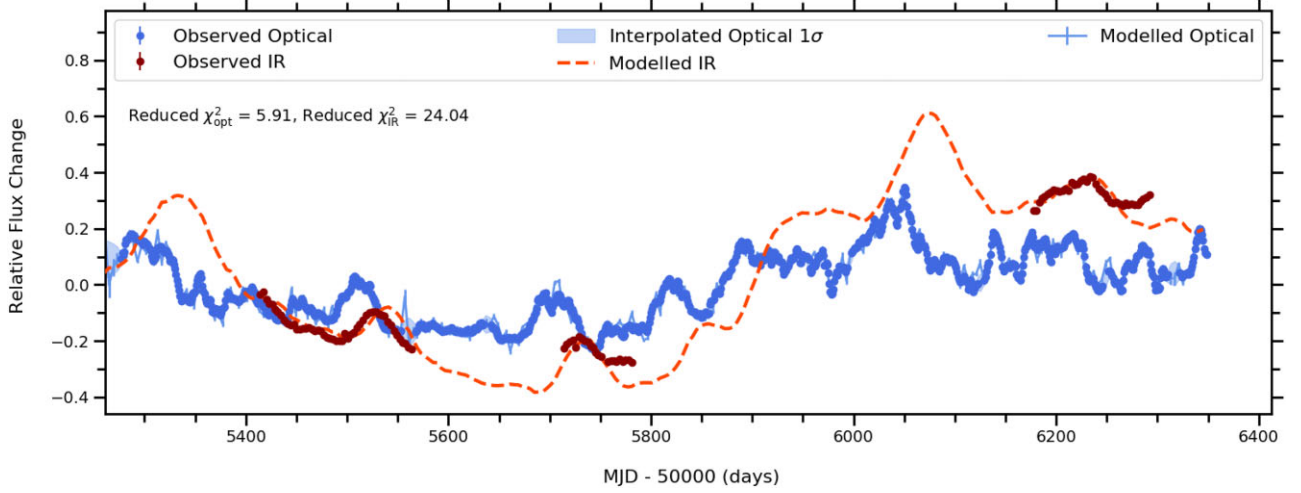


Figure 7. Simulated light curves of *Kepler-Spitzer 1* for the entire overlapping observational periods, plotted with the parameters that corresponded to the highest posterior distribution, with values of $\alpha = -0.50$, $\beta = 0.20$, $w_{\text{eff}} = 2.67$, $\tau = 15.94$ d, and $i = 54.08^\circ$.

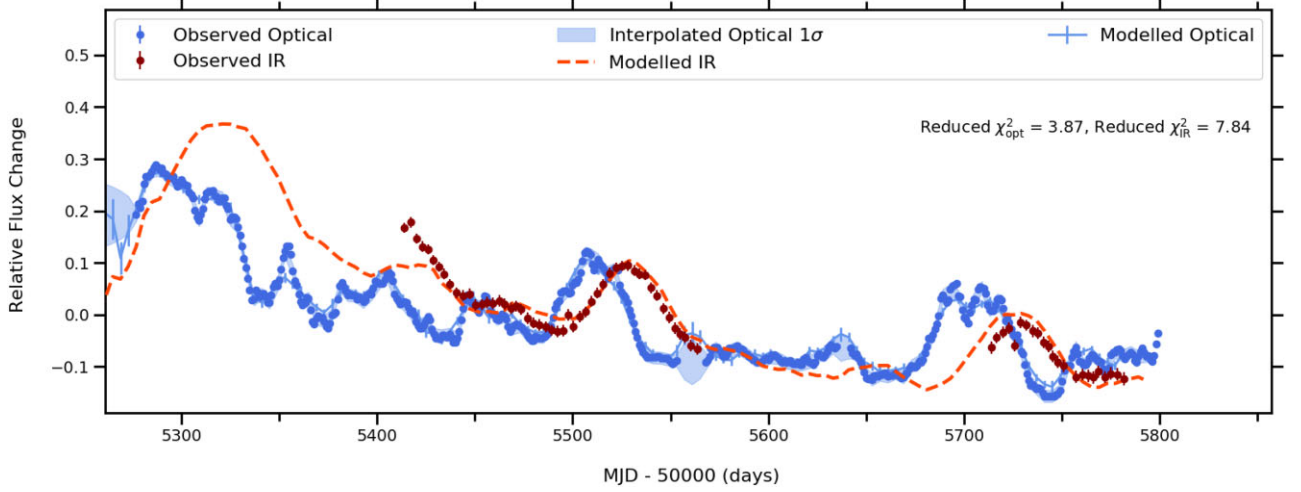


Figure 8. Simulated light curves of *Kepler-Spitzer 1* for the observation seasons starting 2010–2011, plotted with the parameters that corresponded to the highest posterior distribution, with values of $\alpha = -0.56$, $\beta = 0.51$, $w_{\text{eff}} = 1.63$, $\tau = 12.12$ d, and $i = 45.67^\circ$.

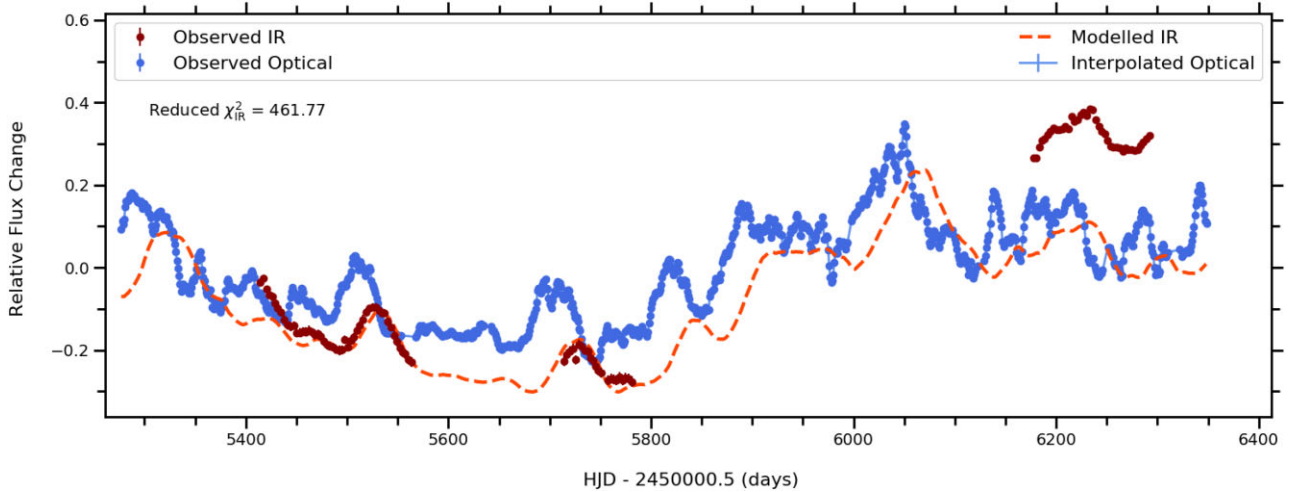


Figure 9. Simulated IR light curve of *Kepler-Spitzer 1* for the entire overlapping observational periods, made using the linearly interpolated *Kepler* light curve convolved with the DTF corresponding to Fig. 8.

Table 2. Mean output parameters of the MCMC modelling for each combination of optical [ground (gr) and *Kepler* (kep)] and IR [*Spitzer* 1 (sp1) and *Spitzer* 2 (sp2)] light curves covering multiple observation seasons that have been separated to exclude the increase in flux between 2011 and 2012. The uncertainties here represent the 1σ standard deviations of the distributions for each parameter in each model. In this table, values of the offset have been multiplied by 10^2 .

Light-curve combination	Seasons starting	Vertical scale		Amplitude conversion factor	Lag (d)	Inclination (deg)	Offset	χ_{opt}^2	χ_{IR}^2
		Radial power-law index	height power-law index						
Gr-Sp1	2010–2011	$-0.52^{+0.01}_{-0.11}$	$0.16^{+0.48}_{-0.10}$	$2.66^{+0.16}_{-0.21}$	$8.02^{+2.16}_{-0.55}$	$49.71^{+13.81}_{-8.83}$	$-0.74^{+0.55}_{-0.40}$	7.87	7.66
Gr-Sp1	2012–2014	$-0.52^{+0.01}_{-0.03}$	$0.23^{+0.45}_{-0.18}$	$1.65^{+0.07}_{-0.06}$	$26.67^{+2.06}_{-1.71}$	$47.76^{+20.42}_{-6.76}$	$1.19^{+0.25}_{-0.23}$	5.99	8.74
Kep-Sp1	2010–2011	$-0.52^{+0.02}_{-0.05}$	$0.08^{+0.51}_{-0.02}$	$1.58^{+0.12}_{-0.10}$	$10.83^{+1.05}_{-1.38}$	$46.68^{+18.81}_{-11.28}$	$0.47^{+0.38}_{-0.38}$	3.87	7.84
Gr-Sp2	2013–2014	$-0.53^{+0.02}_{-0.51}$	$0.08^{+0.53}_{-0.02}$	$1.21^{+0.05}_{-0.04}$	$28.54^{+0.44}_{-5.66}$	$52.09^{+15.75}_{-7.70}$	$0.95^{+0.33}_{-0.22}$	5.19	5.20

4.3.2 Comparing with models of the individual observation seasons

As the time lag increases when modelling the multiseason light curves using the later seasons, the individual observation season light curves were also modelled in Appendix C3.2 (supplementary material) to see whether a change in the parameters was detected over time. The means of the output DTF parameters for these individual season models are compared with the output parameters from the simulated light curves covering multiple observational seasons in Fig. 10, for the radial power-law index, vertical scale height power-law index, time lag, and inclination angle. Comparisons of the output parameters for the optical–IR amplitude conversion factor, and the offset are given in Fig. C13.

It can first be seen that modelling of the individual seasons is not able to constrain the parameters as well as the multiseason plots, specifically for the radial power-law index and the vertical scale height power-law index which often have uncertainties that cover nearly the entire prior range $-5.5 \leq \alpha \leq -0.5$ and $0.05 \leq \beta \leq 2.05$, respectively. This could be a result of the length of the observations, especially as some individual seasons only cover a range of ~ 60 d, which might not be long enough to properly constrain the parameters of the DTFs. Despite the large range in uncertainties, the overall mean is found to be $\alpha = -0.80^{+0.28}_{-0.66}$ and $\beta = 0.23^{+0.35}_{-0.14}$, consistent with the multiseason models.

Similarly, in Fig. 10(d), the inclination angles found for the individual seasons often have a broad spread, with uncertainties covering $\sim 20^\circ$ – 40° , showing that they are not very well constrained. Most combinations of optical and IR light curve are shown to be consistent amongst themselves over the different observation seasons, and the overall mean inclination angle is found to be $i = 49.08^{+2.89}_{-13.17}$ deg. However, some models deviate from this value; for example, the *Kepler-Spitzer* 1 light curves in the 2012 season find a value of $i \approx 20^\circ$, which again could be a result of the length of the individual seasons not being sufficient to properly constrain the parameters. It can also be seen that the value of the inclination angle that corresponds to the highest posterior distribution in the 2014 season of the ground-*Spitzer* 1 light curve is outside of the 1σ uncertainties, which could imply that for this season the MCMC modelling does not search the appropriate range of priors well.

Finally, in Fig. 10(c), the time lags are found to be better constrained in most of the individual observation seasons than the other parameters, especially in the earlier observation seasons. In all individual observation seasons these lags are found with values between ~ 10 and 20 d for the ground-*Spitzer* 1 and *Kepler-Spitzer* 1 light curves, but the ground-*Spitzer* 2 light curves in the 2013 and 2014 seasons find a higher lag of ~ 25 – 30 d, which could be

influencing the larger lag found in ground-*Spitzer* 2 combined 2013–2014 light curves. However, the corresponding ground-*Spitzer* 1 light curves in the individual seasons all find a shorter lag with a value of 10–15 d, although the 2014 season lag has large uncertainties, while the ground-*Spitzer* 1 light curve over the combined 2012–2014 seasons finds the larger lag. Appendix C3.2 (supplementary material) explores these larger uncertainties in the time lag in the later seasons and finds that the models actually return double-peaked distributions for the time lag with peaks at ~ 10 and 30 d. When plotting the models corresponding to the individual peaks, the model for the ~ 10 d lag is shown to better replicate the shape of the variability of the IR observations, but the larger lag has a lower reduced χ^2 value. If the increase in time delay is then not a result of the variability in the individual seasons, the difference between the individual and multiple season models could alternatively still be impacted by modelling their long-term variability and the months-long gaps between observations. The overall mean time lag is found with a value of $\tau = 12.89^{+14.54}_{-2.83}$ d, or for each combination of optical and IR light curve, the means have values of $11.19^{+1.73}_{-2.97}$ d, $11.04^{+5.99}_{-0.29}$ d, and $27.66^{+0.47}_{-0.04}$ d for the ground-*Spitzer* 1, *Kepler-Spitzer* 1, and ground-*Spitzer* 2 light curves, respectively.

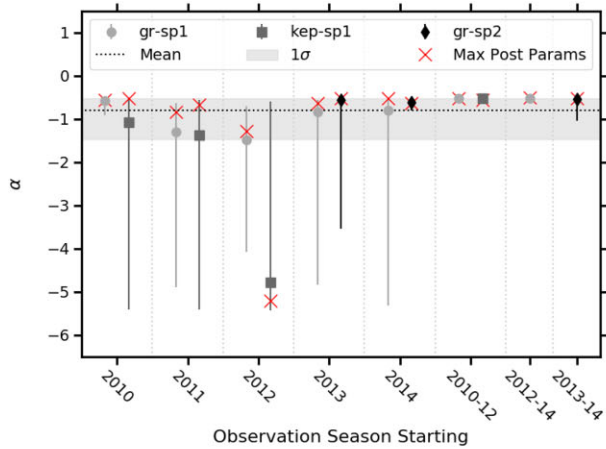
Using the mean radial power-law index, vertical scale height power-law index, and inclination angle from modelling the light curves of Zw229-015, the distribution of dust clouds and the associated delay and illumination maps are plotted in Fig. 11.

5 DISCUSSION

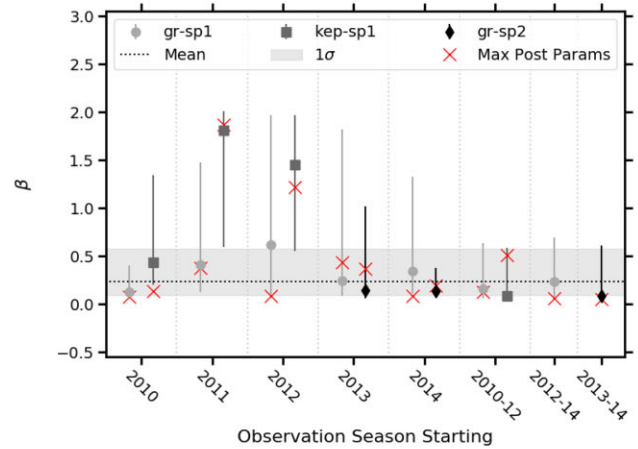
In the previous sections, optical and IR light curves of Zw229-015 were studied to further understand the inner regions of the AGNs that are not spatially resolved.

5.1 Dust reverberation mapping

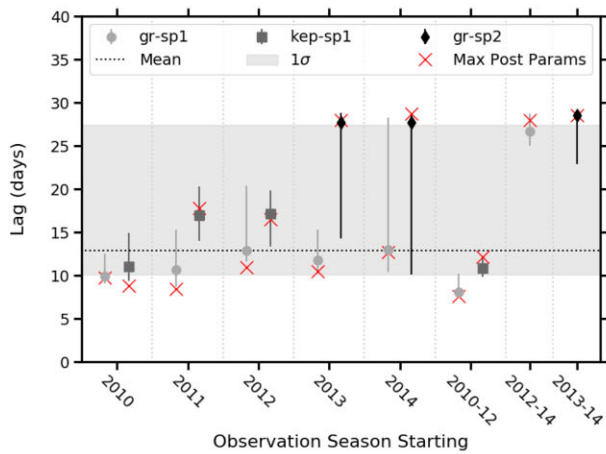
The optical ground-based and *Kepler* light curves were cross-correlated with the IR *Spitzer* channel 1 ($3.6 \mu\text{m}$) and channel 2 ($4.5 \mu\text{m}$) light curves to determine the possible lags between them, and their corresponding dust reverberation radii. The most consistent observed lag was detected between 5 and 30 d in 70 per cent of the CCFs, with an overall mean of $\tau_{\text{obs}} = 18.8 \pm 4.6$ d, which corresponds to a radius of 0.016 ± 0.004 pc (or in the rest frame of Zw229-015, $\tau_{\text{rest}} = 18.3 \pm 4.5$ d, which corresponds to a radius of 0.015 ± 0.004 pc). Additional less-consistent lags were also detected in multiple seasons in the different combinations of optical–IR light curves, including a lag between 55 and 80 d; however, a peak in the corresponding optical ACF in these seasons was detected at ~ 60 d,



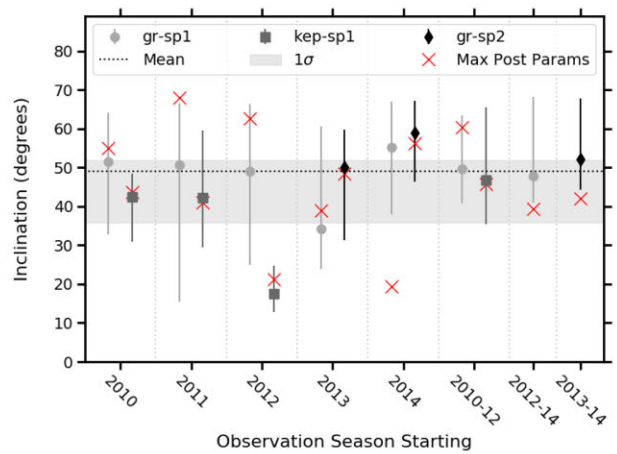
(a) Comparison between the mean output radial power-law indices.



(b) Comparison between the mean output vertical scale height power-law indices.



(c) Comparison between the mean time lags.



(d) Comparison between the mean output inclination angles.

Figure 10. Comparison between the mean output parameters of the MCMC modelling of each combination of optical and IR light curves, for the individual observation seasons and multiseason light curves. The values corresponding to the maximum posterior distribution are also plotted in red.

implying that the lag is not between optical and IR light curves but is a result of aliasing in the light curves. This peak in the optical ACFs is further investigated as a possible periodicity in Appendix B3 (supplementary material); however, it was found to be a result of the overlapping light-curve regions used for cross-correlation, as the entire *Kepler* light curves for each season did not display this peak, nor did the 2013 ground-based light curve or the overall ground and *Kepler* light curves.

The *Spitzer* channel 1 and 2 light curves were also cross-correlated with each other to look for possible lags between the emission from different IR wavelength ranges. The most consistent lag which was detected in all CCFs was found between 0 and 5 d, with a mean of $\tau_{\text{obs}} = 1.8 \pm 1.7 \text{ d}$ ($= \tau_{\text{rest}}$). This ~ 0 lag implies that the 3.6 and 4.5 μm light is dominated by emission from the same dust component. This delay was further investigated in the ground-*Spitzer* 1 and ground-*Spitzer* 2 CCFs. In the 2013 season, a lag was only detected in the RM-ICCF method of ground-*Spitzer* 2, but comparing this with the ground-*Spitzer* 1 shows that the 4.5 μm lag is longer by ~ 13 d; however, this could

be due to the broad nature of the CCFs and the corresponding ACFs, which is explored further in Appendix B2.1 (supplementary material). Furthermore, comparing the lags detected in the 2014 season of the ground-*Spitzer* 1 and ground-*Spitzer* 2 CCFs shows that they are consistent with each other in the individual methods within 1σ .

5.1.1 IR wavelength dependence on dust lags

The mean observed lag is found to be consistent between each combination of optical and IR light curves, and also with the rest-frame delay of $20.36^{+5.82}_{-5.68} \text{ d}$ measured between the V and K_s bands using observations from 2017–2018 by Mandal et al. (2021).

Lyu et al. (2019) found the radius of DRM with longer IR wavelengths to be larger than those of smaller IR wavelengths, as they found a ratio between the K (2.2 μm), W1 (3.4 μm), and W2 (4.5 μm) dust reverberation radii of $R_K : R_{W1} : R_{W2} = 0.6 : 1.0 : 1.2$ for 17 quasars in the K and W1, and 67 quasars in the W1 and W2. Our results show anomalous behaviour for Zw229-015 in comparison to the results

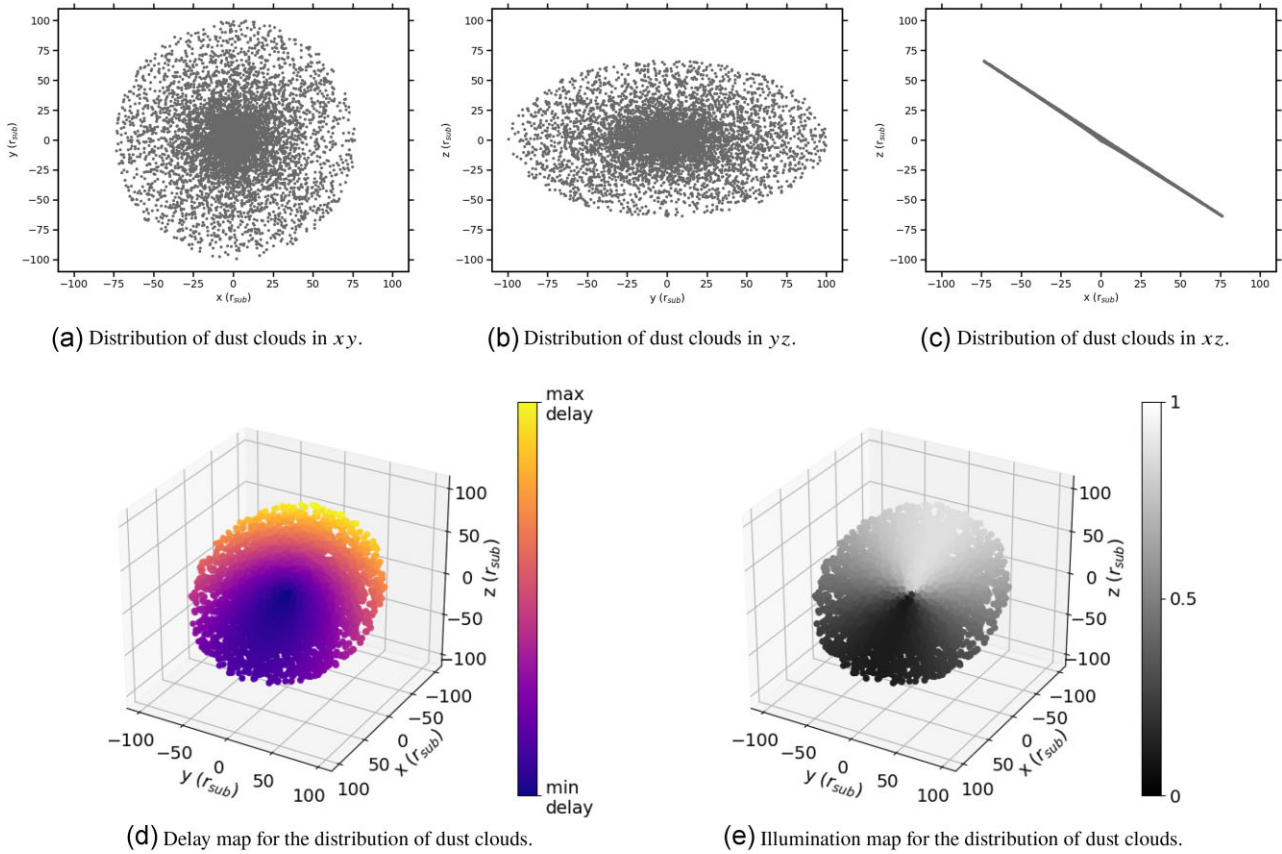


Figure 11. Distribution of 10 000 dust clouds corresponding to the mean parameters from the MCMC modelling of the Zw229-015 light curves, and the corresponding delay and illumination maps.

reported in Lyu et al. (2019); however, as the lags between the optical and $3.6\ \mu\text{m}$, and the optical and $4.5\ \mu\text{m}$ are shown to be consistent within the 1σ uncertainties of the rest-frame dust reverberation lag measured between the V and K_s bands using observations from 2017 to 2018 by Mandal et al. (2021). If we assume that the V and K_s reverberation lag remained approximately consistent in 2010–2018, the similarities between the K_s band ($2.15\ \mu\text{m}$), $3.6\ \mu\text{m}$, and $4.5\ \mu\text{m}$ reverberation lags indicate that in Zw229-015 they are all tracing the same regions, which corresponds to the hottest dust at the inner radius of the dust emitting region. Hönig & Kishimoto (2011) explain that the NIR emission (i.e. the K_s band) predominantly originates in the peak of the blackbody emission of the hot dust in the inner region, while the predominant source of MIR emission (i.e. the 3.6 and $4.5\ \mu\text{m}$ bands) can be either from the peak of the blackbody emission of cooler dust at larger distances from the central engine than the hot dust, or from the Rayleigh–Jeans tail of the hot-dust emission in the inner regions. If the object is compact, and the brightness distributions are therefore steep, the Rayleigh–Jeans tail of the hot-dust emission can dominate the MIR because of the lack of extended dust. This therefore suggests that in the previous MIR reverberation studies that found a larger lag between the optical and MIR than the optical and NIR (e.g. Lyu et al. 2019), the MIR emission is originating in the peak of the blackbody emission of the cooler dust, whereas for Zw229-015, where the lag between the optical and MIR is consistent with the lag between the optical and NIR, the 3.6 and $4.5\ \mu\text{m}$ emission is dominated by the Rayleigh–Jeans tail of the hottest dust.

5.1.2 Comparison with BLR lags

The dust reverberation lag measured in this paper is found to be a factor of ~ 4.7 larger than the BLR reverberation lag measured by Barth et al. (2011), consistent with the results found by Koshida et al. (2014), in which the reverberation radius of broad emission lines is a factor of 4–5 smaller than dust reverberation radii.

Czerny & Hryniewicz (2011) proposed that some broad emission lines are formed in a failed radiatively accelerated dusty outflow, and therefore predict the existence of a significant amount of dust within the BLR. This could be tested with the high-quality optical and IR data used in this paper, which allows for the detection of lags between light curves on time-scales as short as ~ 3 d, consistent with the BLR lag measured by Barth et al. (2011). As a lag on such time-scales is not measured in the high-cadence CCFs, it suggests that the presence of a significant amount of dust in the BLR is unlikely.

5.1.3 Reverberation lag–luminosity relations

Both the dust reverberation radii and BLR reverberation radii are expected to correlate with the optical luminosity of the AGNs, with an approximate relationship of $r \propto L^{1/2}$. For example, Fig. 12(a) shows a plot of R_{BLR} versus optical $5100\ \text{\AA}$ luminosity for Zw229-015 and for other AGNs taken from the literature (Barth et al. 2011; Bentz et al. 2013). For the AGNs in Bentz et al. (2013), the $H\beta$ BLR radius–luminosity relation was found to be $R_{\text{BLR}} \propto L^{0.533^{+0.035}_{-0.033}}$. Additionally, Fig. 12(b) demonstrates the R_{dust} versus the V -band luminosity

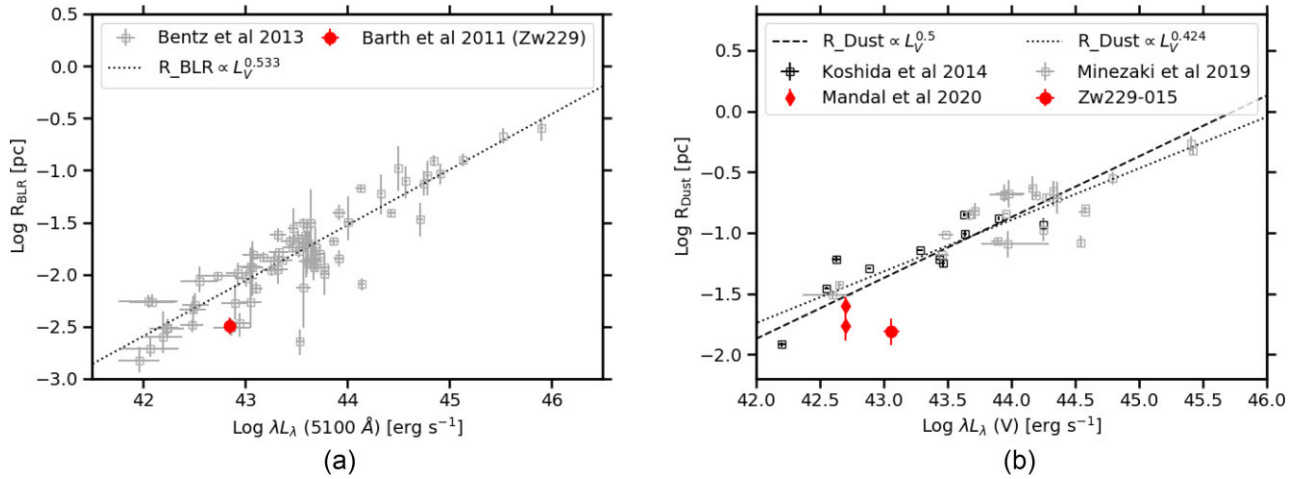


Figure 12. Radius–luminosity relations using AGNs from the literature compared to Zw229-015. (a) Plot of the radius of the BLR against 5100 Å luminosity for AGNs from Bentz et al. (2013) in the black squares and for Zw229-015 using the BLR-RM result from Barth et al. (2011) in red. (b) Plot of the radius of the dust emitting region against V-band luminosity for AGNs from the literature in the black squares (Koshida et al. 2014; Minezaki et al. 2019) and for Zw229-015 using the DRM result from this paper and from Mandal et al. (2021) in red.

relationship using the DRM lag estimated for Zw229-015 in this paper and for other AGNs taken from the literature (e.g. Koshida et al. 2014; Minezaki et al. 2019). Minezaki et al. (2019) fit the luminosity–dust radius relationship of the dust reverberation mapped AGNs from their work and Koshida et al. (2014), both forcing a fixed slope of 0.5 and allowing the slope to vary which resulted in a best fit to the data of $R_{\text{dust}} \propto L^{0.424 \pm 0.026}$. Furthermore, Gravity Collaboration (2020) estimated the hot dust radius versus bolometric luminosity relation using NIR interferometric measurements, and found a best fit with a flatter slope of $R_{\text{dust,int}} \propto L_{\text{bol}}^{0.40 \pm 0.04}$. Alternatively, Lyu et al. (2019) perform a MIR reverberation mapping study of 87 quasars, and find radius–luminosity relationships with slopes of $R_{\text{dust}} \propto L_{\text{bol}}^{0.47 \pm 0.06}$ and $R_{\text{dust}} \propto L_{\text{bol}}^{0.45 \pm 0.05}$ in the W1 (3.4 μm) and W2 (4.5 μm) bands, respectively, which are both consistent with the theorized relationship of $r \propto L^{1/2}$ within their 1σ uncertainties. It is therefore currently unclear whether the deviation of the slope from the relationship of $r \propto L^{1/2}$ is an intrinsic effect: Selection biases could also affect the results as the brightest and most suitably variable objects are typically chosen as targets for both reverberation mapping and interferometric analysis. As it is easier to measure shorter lags in brighter objects, this could therefore lead to a biased selection on the short-lag side from the intrinsic dispersion in the correlation and, hence, flatten the observed slope. Indeed, comparing the distribution of AGN luminosities in Figs 12(a) and (b), it can be seen that fewer dust lags of AGNs with lower luminosity have been recorded, which means the dust plot could be biased by selection effects from selecting mostly more luminous AGNs. Having fewer AGN dust lags for sources with luminosities $\lesssim 10^{43.5} \text{ erg s}^{-1}$ could suggest that the entire distribution of AGNs might not be sampled in this plot. This could be further implied as the dispersion of AGNs from Koshida et al. (2014) and Minezaki et al. (2019) from the radius–luminosity relations at a luminosity of $\sim 10^{44} \text{ erg s}^{-1}$ is greater than at a lower luminosity of $\sim 10^{42.5} \text{ erg s}^{-1}$. Alternatively, selection biases could also result in steeper observed slopes than predicted. For example, AGNs with lower continuum luminosities are likely to contain stronger broad and narrow emission lines compared to the continuum brightness (the Baldwin effect; Baldwin, Wampler & Gaskell 1989). Due to the stronger emission line contributions,

the continuum luminosities inferred from the broad-band imaging filters of these lower luminosity objects could be greater than would be predicted for their measured radii with the expected relationship of $r \propto L^{1/2}$. As this has a greater impact on the lower luminosity objects than the higher luminosity sources, it could therefore potentially lead to a steeper observed relationship between luminosity and radius.

As mentioned above, there are reasons to expect some intrinsic dispersion shown about the best-fitting trends in both Figs 12(a) and (b). Several factors have been considered to explain the dispersion in the distributions. First, the accretion rate of the AGNs affects the slope of the $R_{\text{BLR}}-L$ relationship. Du et al. (2016) showed that AGNs with higher dimensionless accretion rates and higher Eddington ratios have been linked to shorter H β lags, which is theorized to be a result of self shadowing effects of slim ADs (Li, Yuan & Cao 2010). The self-shadowing region suppresses the ionizing flux seen by the BLR clouds (Wang et al. 2014), thereby reducing the ionization parameter at a given distance compared to a normal accretion flow. This leads to a shorter time lag than implied by the luminosity based on the standard relation. Such self-shadowing is not restricted to the BLR, but would also affect dust temperature and, hence, reduce the sublimation radius. As a consequence, a high accretion rate AGNs would have a shorter dust time lag. Secondly, the intrinsic scatter of the $R_{\text{dust}}-L$ relation could be due to the distribution of the dust, and whether it is illuminated isotropically or anisotropically by the central AGNs (Kawaguchi & Mori 2010, 2011; Almeyda et al. 2017, 2020). Kawaguchi & Mori (2010) show that for an AD emitting less radiation in the equatorial plane than towards the poles, the dust sublimation radius would be closer to the central black hole than if the emission was isotropic. Therefore, for AGNs observed along angles closer to the pole, a higher luminosity would be inferred and the measured radius would be smaller compared to predictions using this luminosity. Furthermore, most of the lags in Fig. 12(b) are measured using a constant spectral index to correct the NIR fluxes for contributions from the AD, though AGNs often demonstrate spectral variability as the flux variations are not necessarily consistent across different wavelength ranges (e.g. Kishimoto et al. 2008). Mandal et al. (2021)

therefore suggest that use of constant spectral index could affect the estimated lags. In their analysis with a constant spectral index, their estimated lag is found to lie closer to the predicted relation as shown in Fig. 12(b). Alternatively, a significant increase in brightness of the AGNs is expected to result in a change in the dust sublimation radius as the dust in the innermost region is destroyed; however, the changing sublimation radius is found to follow the brightening with a delay of a few years. For example, Kishimoto et al. (2013) found that the radius at a given time was correlated not with the instantaneous flux but with the long-term average flux of the AGNs in the previous ~ 6 yr.

The results for Zw229-015, both from this paper and from literature, were compared to the $R_{\text{dust}}-L$ and $R_{\text{BLR}}-L$ relations. To put our dust lag measurements into context, we calculate a predicted lag using the correlation found by Minezaki et al. (2019). We determine a mean luminosity of Zw229-015 using the Galactic extinction-corrected ground-based V -band light curves. The predicted time lag was found to be ~ 60 d, which is a factor of ~ 3 larger than the results measured in this paper. Using the theoretical $L^{1/2}$ relation leads to a similar offset. This deviation from the predictions of both the $R_{\text{dust}} \propto L^{1/2}$ and $R_{\text{dust}} \propto L^{0.424}$ relations can be seen in Fig. 12(b), in which R_{dust} is plotted against the V -band luminosity using the DRM lag estimated for Zw229-015 in this paper and for other AGNs taken from the literature (e.g. Koshida et al. 2014; Minezaki et al. 2019). Furthermore, the observed IR lag–luminosity relation of Zw229-015 from Mandal et al. (2021) is also plotted, using both a varying index of the power law for each epoch to estimate the contribution of emission from the AD to the IR light curve, and using a fixed power-law index. Note that the luminosity of Zw229-015 in Mandal et al. (2021) was calculated from a modelled host-galaxy-flux-subtracted light curve, whereas our data point is still expected to have contributions from the host-galaxy flux. Additionally, the predicted BLR time delay estimated using the relation from Bentz et al. (2013) for the optical 5100 Å luminosity of Zw229-015 is found to be ~ 9 d, which is a factor of ~ 2.5 larger than the delay measured by Barth et al. (2011). Fig. 12(a) shows that the measured BLR radius of Zw229-015 is below the $R_{\text{BLR}} \propto L^{0.533}$ relation found by Bentz et al. (2013); however, other objects are also shown to have a similar offset from this relation, which has been suspected to be Eddington ratio dependent (e.g. Du et al. 2016).

Both Figs 12(a) and (b) show that the Zw229-015 BLR and dust lags are consistently shorter than predicted by the canonical lag–luminosity relations. As previously mentioned, a recent change in intrinsic luminosity could cause this deviation if the sublimation radius did not adjust to this change yet. For that, we compare the fluxes used in this paper with photometric monitoring taken at earlier epochs. Zw229-015 was observed with the Catalina Real-time Transient Survey between 2005 and 2010 (e.g. Drake et al. 2009) with the observed V band photometry given in Appendix A (supplementary material). The observed magnitudes did not change substantially over the 5 yr prior to the data used in this paper. Using the observationally inferred typical delay time for structural changes (Kishimoto et al. 2013), we conclude that a substantial increase in brightness is not responsible for the short time lags measured. Two further potential reasons for a deviation from the relation we introduce above are Eddington ratio or anisotropy. Zw229-015 has been previously estimated to have a relatively low accretion rate (Smith et al. 2018) and an inclination angle of $i = 32.9^{+6.1}_{-5.2}$ deg (Williams et al. 2018). This inclination is quite typical for type 1 AGNs and Du et al. (2016) associate offsets from

the BLR lag–luminosity relation to high accretion rates, not low ones.

5.2 Light-curve modelling

The response of the IR dust emission to the optical variability was simulated and compared to observations for each combination of optical and IR light curve of Zw229-015 in an attempt to further constrain the properties of the inner regions of the AGNs, including the distribution of dust, time lag between light curves, and inclination angle of the system. MCMC modelling was used to find the best-fitting DTF that, when convolved with a driving optical light curve, best replicated the variability of the IR emission.

This modelling was initially performed on the entire overlapping light curves; however, Section 4.3 demonstrates that the increase in flux between the 2011 and 2012 seasons in the IR is not well replicated when modelling to fit the shape of the individual seasons in the light curves using a single dust component. The underestimation of the IR flux in the 2012 season could therefore imply that a secondary dust component is contributing to the overall emission, which has previously been seen in other AGNs. For example, Gravity Collaboration (2021) show that ~ 5 per cent of the total flux of NGC 3783 in the K band is located 0.6 pc away in projected distance from the central hot dust component, and they interpret this component as a cloud of dust and gas that is heated by the central AGNs. To lessen the impact of the dramatic increase in flux on the results, the modelling was instead performed on the different combinations of optical and IR light curves in the 2010–2011 seasons and the 2012–2014 seasons separately. Furthermore, to examine whether the parameters corresponding to the best-fitting DTFs were consistent over time, the modelling was also performed on the individual observation seasons. It was found that the parameters were less well constrained for the individual seasons compared to the multiseason plots, which could be due to the length of the observations of individual season light curves, but for the most part the results were consistent with the multiseason models.

The radial power-law index was consistently found to be shallow in all of the models except the *Kepler-Spitzer* 1 2012 season, and had a mean value of $-0.80^{+0.28}_{-0.66}$, which implies that the dust distribution is extended. This result contradicts the results from DRM which suggested that the dust should be compact, as the MIR and NIR lag the optical with similar delays, implying that they are tracing the same hot-dust region. An additional contribution to the total IR emission from another dust component located farther away from the central source could explain this, as the modelling could be influenced by the extended nature of the second component and therefore find the overall dust distribution to be extended. For example, multiple dust components were found by Lyu & Rieke (2021), who analysed dust reverberation signals over a wavelength range of 1–40 μm for NGC 4151, and detected lags corresponding to the sublimation radii of carbon and silicate dust, as well as a lag for cooler dust located farther from the central source.

A low value was consistently found for the vertical scale height power-law index in a majority of models, with a mean value of $\beta = 0.23^{+0.35}_{-0.14}$, which indicates the dust is distributed in a relatively flat disc. García-Burillo et al. (2021) showed that AGNs with low Eddington ratios and/or luminosities are dominated by the disc and thought to display little to no polar dust emission as the radiative pressures are not enough to drive winds, which is observationally confirmed by Alonso-Herrero et al. (2021). Zw229-015 has an Eddington ratio of 0.125 and a bolometric luminosity of $\sim 10^{44}$ erg s $^{-1}$

(Smith et al. 2018), which is therefore consistent with a small vertical scale height power-law index obtained from the modelling.

The time delay that corresponds to the light-traveltime between the source of the optical and IR dust emission was consistently measured for a majority of models with values of ~ 10 – 20 d, and the overall mean time lag was found to be $12.89^{+14.54}_{-2.83}$ d, consistent with the result found with the DRM in Section 3. However, it was also found that all of the simulated ground-*Spitzer* 2 light curves and the ground-*Spitzer* 1 light curves that covered a combination of observation seasons in 2012–2014 detected larger time lags with values approaching the upper limit of the prior range of ~ 25 d. The larger lags in the ground-*Spitzer* 2 models could imply that the lag is different for the 3.6 and 4.5 μm light curves; however, for the individual seasons the uncertainties cover a broad range of lags. These large uncertainties are explored further in Appendix C3.2 (supplementary material), where they are shown to be due to a double-peaked distribution, with peaks at ~ 10 and 30 d. A similar double-peaked distribution of lags is also found in the ground-*Spitzer* 1 light curve in the 2013 season; however, the ~ 10 d peak is stronger for this model. In Fig. C12, both best-fitting models corresponding to each of the peaks in the lag distribution of the ground-*Spitzer* 2 2014 season are plotted, and it is shown that the model corresponding to the ~ 10 d lag follows the shape of the variability of the IR observations better, though the reduced χ^2 is smaller for the ~ 30 d lag model. The larger lag found in some of the individual season models, especially in the ground-*Spitzer* 2 but also in the 2013 ground-*Spitzer* 1 light curve, could therefore influence the larger lag found in the multiseason models in 2012–2014. Additionally, the modelling over these seasons could still be impacted by the long-term variability, or as a result of the large gaps between observations.

Finally, the mean inclination angle found by modelling the light curves was $49.08^{+2.89}_{-13.17}$ deg, which is consistent with the inclination angle measured by Williams et al. (2018) of $i = 32.9^{+6.1}_{-5.2}$ deg and Raimundo et al. (2020) of $i = 36.4^{+6.7}_{-6.4}$ deg within 1σ .

5.2.1 Limitations of the dust transfer function simulations used in modelling the IR light curves in response to the optical emission

In this paper, DTFs are simulated using a simplified model of a clumpy dust distribution. Specifically, this model includes a distribution of dust clouds with both radial and vertical components. For further simplification, the dust clouds are assumed to be uniform in size, each with the same composition, and the effects of the geometrical distribution of dust, as well as orientation and illumination are considered when simulating the DTFs. To create a more realistic model of the dust distribution, however, further complex effects would need to be considered.

For example, it is assumed that the observed emission from the dust clouds comes from the surfaces directly illuminated from the central engine, and that the emission from each dust cloud is not attenuated by other dust clouds along the line of sight to the observer. In reality, however, as the dust clouds are believed to be optically thick, some clouds could have the line of sight to the central source blocked by others (referred to as ‘cloud shadowing’). These clouds will therefore not be directly heated by the central engine, but instead will be heated by the diffuse radiation from nearby directly heated clouds. Almeyda et al. (2017) explored the effects of cloud shadowing in their model of the simulated dust emission response to optical emission, and found that cloud shadowing can dramatically effect the transfer functions at wavelengths $< 3.5 \mu\text{m}$. In addition, the

diffuse radiation field should also heat the non-illuminated sides of the dust clouds, which would result in an increase in flux detected by the observer. Furthermore, the line of sight from a given cloud to the observer can be blocked by an intervening cloud (referred to as ‘cloud occultation’). Almeyda et al. (2020) showed that cloud occultation can impact the DTFs, resulting in transfer functions that are more sharply peaked at shorter delays, and have shallower tail decays.

Additionally, in the model used in this paper, the optical continuum is assumed to emit isotropically, and therefore the flux absorbed by each cloud is dependent on the distance of the cloud from the AGNs. As mentioned previously, Kawaguchi & Mori (2010) find that for an AD that emits less radiation in the equatorial plane than towards the poles, the dust sublimation radius would be closer to the central black hole than if the emission was isotropic. Almeyda et al. (2017) consider the effects of anisotropic illumination from the AD and find that DTFs for such illumination models typically peak at shorter lags and exhibit narrower peaks as a result of shorter travel times to the inner clouds that are located nearer to the central engine in the equatorial plane.

Furthermore, a change in sublimation radius of the dust distribution as a result of a significant change in optical emission is not supported in the model used in this paper, though this behaviour is expected to occur in AGNs in a realistic scenario (e.g. Kishimoto et al. 2013). However, as discussed previously, for Zw229-015 the observed magnitudes did not change significantly over the 5 yr prior to the data used in this paper.

6 SUMMARY

We studied the optical and IR variability of Zw229-015, a Seyfert 1 galaxy at $z = 0.028$, using observations from optical ground-based telescopes and the *Kepler* space telescope, and concurrent IR observations from the *Spitzer Space Telescope* at 3.6 and 4.5 μm . The results are summarized as follow:

- (i) We used multiple methods of cross-correlation to measure dust reverberation lags. We found a mean rest-frame lag of 18.3 ± 4.5 d for all combinations of optical and IR light curves, over the entire observation periods and the individual observation seasons.
- (ii) No obvious difference was found between the DRM lags recovered using the *Spitzer* 1 (3.6 μm) or *Spitzer* 2 (4.5 μm) light curves; furthermore, these lags were consistent with the result found between the V and K_s bands measured by Mandal et al. (2021), which implies that the different IR wavelength ranges are dominated by dust within the same emission regions.
- (iii) Measured lags of Zw229-015 are consistently smaller than predictions from the lag–luminosity relations, for both IR dust lags and the BLR lag from Barth et al. (2011).
- (iv) By simulating a simplified, clumpy distribution of dust, the response of the IR dust emission to the optical variability was explored using MCMC modelling to further constrain parameters of the inner regions of the AGNs that are not directly observable.
- (v) An increase in flux between the 2011 and 2012 observation seasons, which is more extreme in the IR light curve than in the optical, was shown to not be modelled well by a single dust component, which could therefore imply that multiple dust components are contributing to the overall emission.
- (vi) The MCMC modelling consistently found that the dust was distributed with a shallow radial power-law index and a relatively

small vertical scale height power-law index, implying an extended, flat dust distribution.

(vii) The modelling also estimated a mean inclination angle of 49_{-13}^{+3} deg, consistent with the inclination angle found by Williams et al. (2018) and Raimundo et al. (2020) within 1σ uncertainties, and also detected a mean projected time lag of $12.9_{-2.8}^{+14.5}$ d, consistent with the result found for the DRM.

ACKNOWLEDGEMENTS

EG and SFH acknowledge support from the Horizon 2020 ERC Starting Grant *DUST-IN-THE-WIND* (ERC-2015-StG-677117). EG is grateful to STFC for funding this PhD work. Research at UC Irvine has been supported by NSF grants AST-1412693 and AST-1907290. AVF's group at UC Berkeley received financial assistance from the TABASGO Foundation, the Christopher R. Redlich Fund, the U.C. Berkeley Miller Institute for Basic Research in Science (where AVF was a Miller Senior Fellow), and numerous individual donors.

This paper includes data collected by the *Kepler* mission and obtained from the MAST data archive at the Space Telescope Science Institute (STScI). Funding for the *Kepler* mission is provided by the NASA Science Mission Directorate. STScI is operated by the Association of Universities for Research in Astronomy, Inc., under NASA contract NAS 5-26555. This work is based in part on observations made with the *Spitzer Space Telescope*, which was operated by the Jet Propulsion Laboratory, California Institute of Technology, under a contract with NASA. The research was partly carried out at the Jet Propulsion Laboratory, California Institute of Technology, under a contract with the National Aeronautics and Space Administration (80NM0018D0004).

This work makes use of observations from the Las Cumbres Observatory global telescope network. KAIT and its ongoing operation were made possible by donations from Sun Microsystems, Inc., the Hewlett-Packard Company, AutoScope Corporation, Lick Observatory, the NSF, the University of California, the Sylvia & Jim Katzman Foundation, and the TABASGO Foundation. Research at Lick Observatory is partially supported by a generous gift from Google.

MDJ thanks the Department of Physics and Astronomy at Brigham Young University for continued support of research efforts at the BYU West Mountain Observatory. Research with the WMO 0.9 m telescope was supported by NSF PREST grant AST-0618209 during the time the observations used in this investigation were secured.

DATA AVAILABILITY

The data underlying this article are available in the article and in its online supplementary material.

REFERENCES

Almeyda T., Robinson A., Richmond M., Vazquez B., Nikutta R., 2017, *ApJ*, 843, 3
 Almeyda T., Robinson A., Richmond M., Nikutta R., McDonough B., 2020, *ApJ*, 891, 26
 Alonso-Herrero A. et al., 2021, *A&A*, 652, A99
 Antonucci R., 1993, *ARA&A*, 31, 473
 Baldwin J. A., Wampler E. J., Gaskell C. M., 1989, *ApJ*, 338, 630
 Barth A. J. et al., 2011, *ApJ*, 732, 121
 Barvainis R., 1987, *ApJ*, 320, 537
 Bentz M. C. et al., 2013, *ApJ*, 767, 149
 Blandford R. D., McKee C. F., 1982, *ApJ*, 255, 419
 Brown T. M. et al., 2013, *PASP*, 125, 1031

Clavel J., Wamsteker W., Glass I. S., 1989, *ApJ*, 337, 236
 Czerny B., Hryniewicz K., 2011, *A&A*, 525, L8
 Drake A. J. et al., 2009, *ApJ*, 696, 870
 Du P. et al., 2016, *ApJ*, 825, 126
 Edelson R., Vaughan S., Malkan M., Kelly B. C., Smith K. L., Boyd P. T., Mushotzky R., 2014, *ApJ*, 795, 2
 Emmanoulopoulos D., McHardy I. M., Uttley P., 2010, *MNRAS*, 404, 931
 Falco E. E. et al., 1999, *PASP*, 111, 438
 Fazio G. G. et al., 2004, *ApJS*, 154, 10
 Filippenko A. V., Li W. D., Treffers R. R., Modjaz M., 2001, in Paczynski B., Chen W.-P., Lemme C., eds, ASP Conf. Ser. Vol. 246, IAU Colloq. 183: Small Telescope Astronomy on Global Scales. Astron. Soc. Pac., San Francisco, p. 121
 García-Burillo S. et al., 2021, *A&A*, 652, A98
 Glass I. S., 1992, *MNRAS*, 256, 23P
 Gravity Collaboration, 2020, *A&A*, 635, A92
 Gravity Collaboration, 2021, *A&A*, 648, A117
 Guise E. et al., 2022, *MNRAS*, 510, 3145
 Hönig S. F., Kishimoto M., 2011, *A&A*, 534, A121
 Hönig S. F., Kishimoto M., Antonucci R., Marconi A., Prieto M. A., Tristram K., Weigelt G., 2012, *ApJ*, 755, 149
 Hönig S. F. et al., 2013, *ApJ*, 771, 87
 Kasliwal V. P., Vogeley M. S., Richards G. T., 2015, *MNRAS*, 451, 4328
 Kawaguchi T., Mori M., 2010, *ApJ*, 724, L183
 Kawaguchi T., Mori M., 2011, *ApJ*, 737, 105
 Kishimoto M., Antonucci R., Blaes O., Lawrence A., Boisson C., Albrecht M., Leipski C., 2008, *Nature*, 454, 492
 Kishimoto M., Hönig S. F., Antonucci R., Kotani T., Barvainis R., Tristram K. R. W., Weigelt G., 2009, *A&A*, 507, L57
 Kishimoto M. et al., 2013, *ApJ*, 775, L36
 Koshida S. et al., 2014, *ApJ*, 788, 159
 Krolik J. H., Begelman M. C., 1988, *ApJ*, 329, 702
 Landsman W. B., 1995, in Shaw R. A., Payne H. E., Hayes J. J. E., eds, ASP Conf. Ser. Vol. 77, Astronomical Data Analysis Software and Systems IV. Astron. Soc. Pac., San Francisco, p. 437
 Leftley J. H., Tristram K. R. W., Hönig S. F., Kishimoto M., Asmus D., Gandhi P., 2018, *ApJ*, 862, 17
 Li G.-X., Yuan Y.-F., Cao X., 2010, *ApJ*, 715, 623
 Lyu J., Rieke G. H., 2021, *ApJ*, 912, 126
 Lyu J., Rieke G. H., Shi Y., 2017, *ApJ*, 835, 257
 Lyu J., Rieke G. H., Smith P. S., 2019, *ApJ*, 886, 33
 Mandal A. K. et al., 2018, *MNRAS*, 475, 5330
 Mandal A. K. et al., 2021, *MNRAS*, 501, 3905
 Minezaki T., Yoshii Y., Kobayashi Y., Enya K., Suganuma M., Tomita H., Aoki T., Peterson B. A., 2004, *ApJ*, 600, L35
 Minezaki T. et al., 2019, *ApJ*, 886, 150
 Nelson B. O., 1996, *ApJ*, 465, L87
 Pancoast A. et al., 2019, *ApJ*, 871, 108
 Pei L. et al., 2014, *ApJ*, 795, 38
 Peterson B. M., 1993, *PASP*, 105, 247
 Peterson B. M., Wanders I., Horne K., Collier S., Alexander T., Kaspi S., Maoz D., 1998, *PASP*, 110, 660
 Pott J.-U., Malkan M. A., Elitzur M., Ghez A. M., Herbst T. M., Schödel R., Woillez J., 2010, *ApJ*, 715, 736
 Pozo Nuñez F. et al., 2015, *A&A*, 576, A73
 Raban D., Jaffe W., Röttgering H., Meisenheimer K., Tristram K. R. W., 2009, *MNRAS*, 394, 1325
 Raimundo S. I., Vestergaard M., Goad M. R., Grier C. J., Williams P. R., Peterson B. M., Treu T., 2020, *MNRAS*, 493, 1227
 Ramolla M. et al., 2018, *A&A*, 620, A137
 Rieke G. H., Lebofsky M. J., 1981, *ApJ*, 250, 87
 Shakura N. I., Sunyaev R. A., 1973, *A&A*, 500, 33
 Shi Y. et al., 2006, *ApJ*, 653, 127
 Shi Y., Rieke G. H., Smith P., Rigby J., Hines D., Donley J., Schmidt G., Diamond-Stanic A. M., 2010, *ApJ*, 714, 115
 Smith K. L., Mushotzky R. F., Boyd P. T., Malkan M., Howell S. B., Gelino D. M., 2018, *ApJ*, 857, 141
 Suganuma M. et al., 2006, *ApJ*, 639, 46

- Swain M. et al., 2003, *ApJ*, 596, L163
Tacconi L. J., Genzel R., Blietz M., Cameron M., Harris A. I., Madden S., 1994, *ApJ*, 426, L77
Tristram K. R. W. et al., 2007, *A&A*, 474, 837
Vazquez B. et al., 2015, *ApJ*, 801, 127
Wang J.-M., Du P., Li Y.-R., Ho L. C., Hu C., Bai J.-M., 2014, *ApJ*, 792, L13
Weigelt G. et al., 2012, *A&A*, 541, L9
Welsh W. F., 1999, *PASP*, 111, 1347
Werner M. W. et al., 2004, *ApJS*, 154, 1
Williams P. R. et al., 2018, *ApJ*, 866, 75
Yoshii Y., Kobayashi Y., Minezaki T., Koshida S., Peterson B. A., 2014, *ApJ*, 784, L11

SUPPORTING INFORMATION

Supplementary data are available at *MNRAS* online.

suppl_data

Please note: Oxford University Press is not responsible for the content or functionality of any supporting materials supplied by the authors. Any queries (other than missing material) should be directed to the corresponding author for the article.

This paper has been typeset from a \TeX/L\AA\TeX file prepared by the author.